Received: 19 February 2024 | Revised: 4 May 2024 | Accepted: 31 May 2024

DOI: 10.1002/msd2.12118

RESEARCH ARTICLE

IJMSD International Journal of Mechanical System Dynamics Open Access WILEY

Nonlinear response of a multidirectional negative-stiffness isolation system via semirecursive multibody dynamic approach

Wei Dai[1] | Biagio Carboni[2] | Giuseppe Quaranta[2] | Yongjun Pan[1] | Walter Lacarbonara[2]

[1]College of Mechanical and Vehicle Engineering, Chongqing University, Chongqing, China

[2]Department of Structural and Geotechnical Engineering, Sapienza University of Rome, Rome, Italy

Correspondence
Prof. Giuseppe Quaranta, Department of Structural and Geotechnical Engineering, Sapienza University of Rome, Via Eudossiana 18, 00184 Rome, Italy.
Email: giuseppe.quaranta@uniroma1.it

Funding information
RETURN Extended Partnership, Grant/Award Number: D.D. 1243 PE0000005; China Scholarship Council, Grant/Award Number: 202206050096; PRIN 2022, Grant/Award Number: 2022TH5HC2; PRIN 2022 PNRR, Grant/Award Number: P20227KKF5

Abstract

This paper investigates an innovative negative-stiffness device (NSD) that modifies the apparent stiffness of the supported structure for seismic isolation. The NSD comprises a lower base on the bottom and a cap on the top, together with a connecting rod, vertical movable wall, and compressed elastic spring, as well as circumferentially arranged, pretensioned external ropes, and inclined shape memory wires. This configuration can deliver negative stiffness and energy dissipation in any direction within the horizontal plane. A numerical model of the device is developed through a two-step semirecursive method to obtain the force–displacement characteristic relationship. Such a model is first validated through comparison with the results obtained via the commercial software ADAMS. Finally, a large parametric study is performed to assess the role and the influence of each design variable on the overall response of the proposed device. Useful guidelines are drawn from this analysis to guide the system design and optimization.

KEYWORDS
multibody system, negative stiffness, semirecursive approach, seismic protection, vibration isolation

1 | INTRODUCTION

Base isolation has proven to be an effective strategy for protecting new and existing buildings against earthquakes. The fundamental idea of base isolation is to decouple the response of the supported structure from its foundation or substructure on the ground. In this way, earthquake-induced relative displacements are primarily confined within the seismic isolation system level, with the superstructure displaying nearly rigid-body motion. The rapid evolution[1–5] and the widespread adoption[6–10] of seismic isolation systems demonstrate their effectiveness in ensuring the required performance levels for buildings in earthquake-prone areas. Elastomeric and sliding bearings are most commonly employed for seismic protection. Elastomeric bearings are assembled by alternating layers of (natural or synthetic) rubber and steel.[11–13] Rubber layers offer lateral flexibility, whereas the steel layers provide vertical stiffness. Additionally, rubber covers are applied on the top, bottom, and sides of the bearing to shield the steel plates. A central lead cylinder can be incorporated to enhance initial stiffness and improve energy dissipation. Sliding bearings commonly employ either spherical or

flat sliding surfaces. The friction pendulum system bearing,[14–17] which utilizes a spherical surface, is the most widely adopted sliding bearing. It typically utilizes a low-friction material, such as polytetrafluoroethylene (PTFE) and stainless steel, for the bearing material at the interface.

Some recent advances in the field of vibration isolation systems deal with the development of bioinspired isolators,[18–21] quasizero or zero stiffness devices,[22–25] and negative-stiffness devices (NSDs).[26–28] Building upon the seminal idea by Molyneux,[29] NSDs are recently attracting increasing attention in vibration isolation. In this context, negative stiffness implies the introduction of a force to promote motion rather than resist it without the need for an external power supply. The negative stiffness in the existing proposals for vibration isolation systems is achieved through energy storage elements, such as preloaded springs and prebuckled beams, as well as magnetic components, geometrically nonlinear structures, composite structures, and metamaterials.[26] Most applications of NSDs for vibration isolation systems are related to industrial engineering, including vehicle seat suspension,[30,31] vehicle suspension systems,[32,33] and railway vehicles.[34,35] Sarlis et al.[36] were among the first who proposed, manufactured, and tested an NSD for seismic isolation of civil structures. This device consists of the following components: a precompressed spring placed in a central position generating negative stiffness; a double chevron self-containing system to counteract the preload in the compressed spring and to prevent the transfer of its vertical component to the structure; a double negative-stiffness magnification mechanism decreasing the preload requirement; a viscous damper to reduce the experienced displacement within acceptable levels; a gap spring assembly delaying the engagement until a threshold displacement is reached. Upon the integration of viscous dampers, such bearing for seismic isolation exhibits a positive influence on the seismic response of the superstructure, efficiently reducing floor accelerations, interstory drift, and base shear, while maintaining isolator displacements within acceptable limits.[37] Cimellaro et al.[38] performed numerical simulations on a seismic isolation system specifically designed to deal with strong vertical ground shaking. The base isolation setup includes elastomeric bearings functioning in both horizontal and vertical orientations, alongside NSDs operating solely in the vertical direction. The inherent damping of rubber isolators in this case was found useful to avoid the introduction of specific dampers in the vertical direction.

Vibration isolation systems with negative stiffness have some advantages compared with standard devices with positive stiffness. In particular, positive-stiffness isolators can exhibit resonance behavior at large period values, which may amplify certain low frequencies rather than attenuate them. Such an issue is especially relevant for buildings located in near-fault areas, where the occurrence of long-period, pulse-like seismic ground motions close to the causative fault can be detrimental to the performance of conventional seismic isolation systems.[39–42] Negative-stiffness isolators can instead overcome this drawback since they achieve very high levels of vibration isolation even at low frequencies. For instance, Chen et al.[43] considered a base isolation system with NSDs where a vertically preloaded helical spring can produce variable restoring force in the lateral direction through geometric nonlinearity. The numerical assessment of such a base isolation system has shown that NSDs are especially promising under near-field earthquakes with pulse-like components. It is important to highlight that almost all proposed NSDs for seismic isolation are effective under unidirectional base motion. This means that several NSDs must be installed in different directions to ensure multidirectional seismic protection of the superstructure. The isolator bearing proposed by Cao et al.[44] can potentially overcome this limitation by including superelastic shape memory alloy (SMA) cables and a frictional sliding bearing featuring convex surfaces. This bearing is able to limit the forces transmitted to the superstructure, enabling supplemental energy dissipation through the SMA cables. Indeed, although isolators with negative stiffness can provide consistent performance across a larger frequency range, their inherent damping is low compared with that of standard positive-stiffness isolators, and thus ad hoc solutions are needed to provide an additional source of energy dissipation.

Parallel to the continuous advances in seismic isolation systems, several numerical approaches have been implemented to simulate their response. To this end, analytical, phenomenological, and finite element models are the most common approaches.[45–47] Only a few studies explored the use of multibody models to simulate the response of seismic isolation systems and none of them included NSDs. By deriving multibody kinematic equations for double-concave curved-surface slider isolators, Bianco et al.[48] pointed out that the common assumption of compliant sliding for such devices is questionable because the fulfillment of geometric compatibility implies a recursive alternation of sticking and slipping. Mezghani et al.[49] developed a multibody model using Matlab Simscape Multibody for a seismic isolator that combines a knitted stainless steel wire cushion with a coil spring. While multibody models are less prevalent in this domain, their ability to closely describe the real working conditions of all components in a seismic isolator enables them to yield accurate results.

Generally, there are various methods for elaborating multibody models. The most widely used approach is the multibody dynamics method based on Cartesian coordinates.[50–52] This method is known for its simplicity and versatility, and many commercial software platforms (such as ADAMS) are based on this approach. However, for large closed-loop multibody systems, the resulting multibody dynamics equations tend to be complex, resulting in relatively lower computational efficiency. Semirecursive multibody dynamic methods have been formulated to lower the complexity of the equations of motion and enhance computational efficiency.[53–55] These methods evolved from the fully recursive multibody formulations based on relative coordinate systems.[56] The generalized semirecursive method[57] and the two-step semirecursive method[58] are regarded as the most representative multibody dynamic modeling approaches.

In this paper, a novel vibration isolation device with negative stiffness is presented and modeled.[59,60] Different from most of the previous proposals, the present device can provide negative stiffness

in any direction, and the presence of SMA wires contributes to energy dissipation. A two-step semirecursive multibody dynamic modeling approach is employed to investigate the nonlinear response of the proposed device and to carry out a comprehensive parametric analysis. The remaining part of this article is organized as follows. Section 2 illustrates the vibration isolation system based on the proposed NSD. The double-step semirecursive modeling approach and the multibody system dynamic model of the proposed NSD are discussed in Section 3. The results of the numerical simulations are presented in Section 4. Herein, the implemented semirecursive model is first validated by comparing its outcomes with the results obtained in ADAMS. Afterward, the outcomes of an extensive parametric study are examined to support the design optimization of the device.

2 | VIBRATION ISOLATION SYSTEM USING NEGATIVE STIFFNESS

A new vibration isolation concept that exploits a novel NSD is investigated in the present work. Figure 1 shows a comprehensive three-dimensional (3D) view of the proposed device in its undeformed configuration together with its main components.

The main components of this NSD include a lower base on the bottom and a cap on the top, while a connecting rod, a vertical movable wall, and an elastic spring are in between. The base is rigidly connected to the ground via bolts and ensures suitable support for the device. The cap is linked to an upper plate by vertical bars designed to slide smoothly within the sleeves on the plate, minimizing friction. A crucial component is the rod that connects the cap and the vertically movable wall, facilitating the transmission of the restoring force from the elastic spring. Featuring spherical heads with low friction at both ends, the rod rotates within corresponding hemispherical grooves in the movable wall and the cap. The movable wall, a disc-shaped slider, moves exclusively in the vertical direction relative to the base. This design ensures the polyurethane (PU) elastic spring deforms solely along its vertical axis, generating a vertical force. Hollow cylinders made of PTFE can be fixed either to the vertical bars or the housings within the upper plate to ensure low friction at the interface between them and secure a smooth sliding. The hemispherical grooves within the movable wall can also be made of PTFE to ensure smooth contact with the steel spherical heads. The friction coefficient for the dry sliding condition between steel and PTFE composite with the addition of 25% in weight of graphite is close to 0.12,[61] although this is a reference value that should be tuned according to the operating temperature, sliding velocity, and surface pressure.

Before the proposed device begins operation, the elastic spring must be precompressed through a set of pretensioned external ropes circumferentially distributed. The ends of the ropes are then connected to the cap and the base, thus maintaining the initial deformation of the elastic spring. The ropes must be manufactured employing high-strength materials, such as NiTi wire strands, so that their length does not change significantly during the device's operation. Additionally, there is a group of oblique (not pretensioned) wires between the cap and the vertical wall. They are distributed according to a circular pattern, with their ends connected to the cap and the vertical movable wall. These metallic wires can be made of SMA to withstand repeated tensile stresses without undergoing detrimental permanent deformations thanks to the superelastic behavior.

Figure 2 illustrates the NSD in three different configurations to better explain its working mechanism. Particularly, the left picture in Figure 2 depicts the NSD at rest, a state in which the elastic spring element has not been compressed yet and the external ropes are in a relaxed state. Afterward, the NSD is precompressed by tensioning the external ropes, as shown in the central picture of Figure 2. The tension force of the ropes is transmitted to the connecting rod through the cap, and then to the vertically movable wall along the connecting rod. Accordingly, the cap moves downward, and the spring deforms under the force exerted by the moving wall until

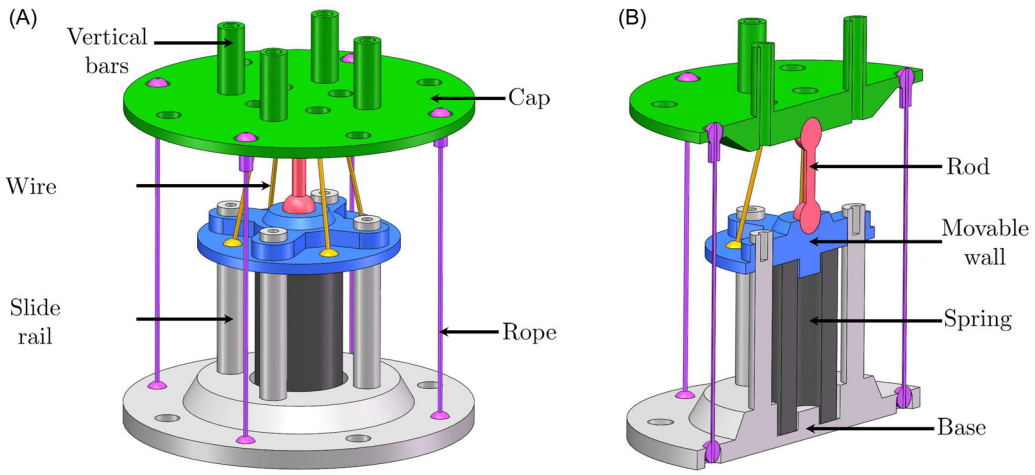

FIGURE 1 Three-dimensional virtual prototype model of the proposed negative-stiffness device: (A) full view and (B) cross-sectional view.

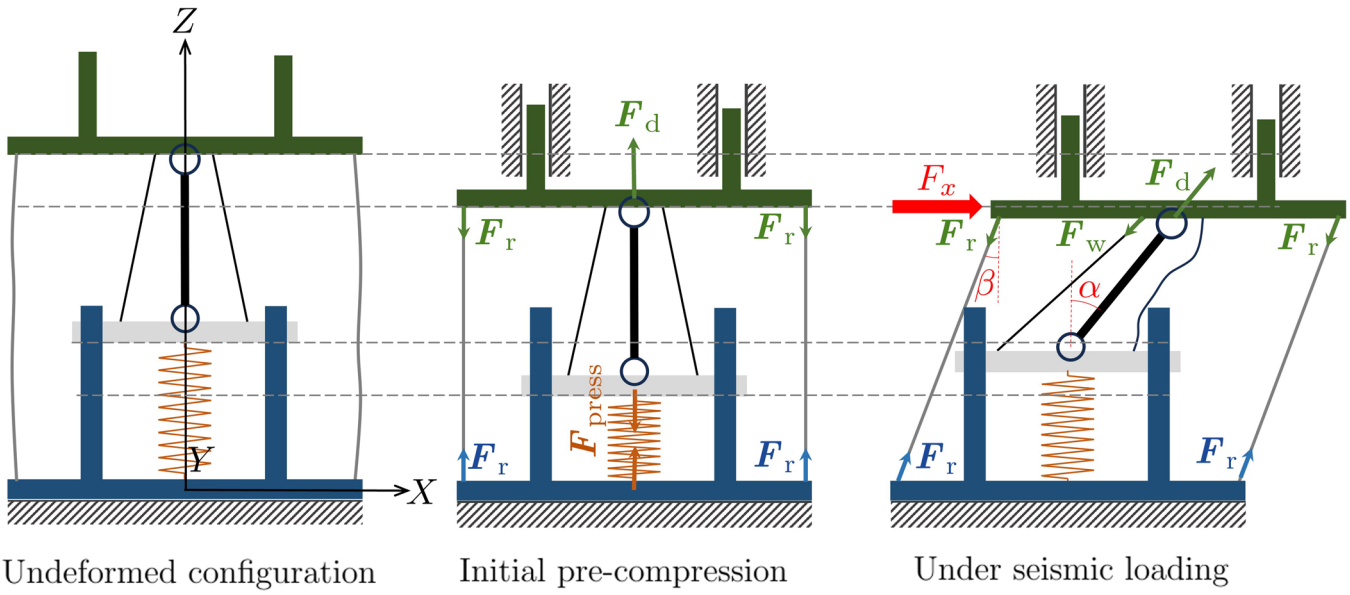

FIGURE 2 Working configurations of the proposed negative-stiffness device.

the system reaches its equilibrium. Once the NSD has been precompressed, the initial working configuration is achieved. It is noted that the connecting rod is now in a state of unstable equilibrium. Hence, the inclined wires are introduced to enhance the stability. When the cap experiences a slight displacement, the diagonal wires on the side opposite to the direction of the cap motion are tightened, generating tension force. This aids the cap in resisting small displacements close to the equilibrium position.

The right picture in Figure 2 finally illustrates the configuration of the NSD in a deformed state due to a lateral input force. The upper cap and the base of the device undergo relative motion, and the connecting rod rotates around its spherical joints. Simultaneously, the wall is carried upward and the connected precompressed elastic spring undergoes extensions. Since the length of the connecting rod is much smaller than the length of the outer ropes, the variation of the inclination angle of the connecting rod is larger than that of the external ropes throughout the motion. This angular difference results in a horizontal component of the rod thrust force $\boldsymbol{F}_{\mathrm{d}}$ applied to the cap greater than the horizontal component of the total traction force $\boldsymbol{F}_{\mathrm{r}}$ generated by the ropes. As a consequence, the resulting horizontal force on the cap is in the direction of motion, helping to drive the system away from the initial position thus generating a negative stiffness. As the relative motion between the upper cap and the base of the device further increases, the tension in the ropes and the precompression force in the elastic element gradually decrease, leading to a gradual reduction of the horizontal resultant force applied on the cap, thereby inducing a positive stiffness.

Thanks to its axial symmetry, the device consistently offers a negative stiffness regardless of the incoming input direction in the horizontal plane. Since the cap is connected to an upper plate via vertical bars that can slide smoothly, negative stiffness governs the device's horizontal behavior while leaving its vertical stiffness unaffected. The oblique wires apply forces that postpone the activation of the device's negative stiffness. This, in turn, enhances the stability of the NSD and contributes to amplifying the equivalent damping.

The analytical expression of the horizontal force provided by the device F_x can be obtained by imposing the balance of the forces in the deformed configuration neglecting the friction forces:

$$F_x = F_{\mathrm{d}} \sin \alpha - \sum F_{\mathrm{w}x} - F_{\mathrm{r}} \sin \beta, \tag{1}$$

where $F_{\mathrm{d}} \sin \alpha$ is the horizontal component of the rod force, whose inclination angle is α (see Figure 2). The term $\sum F_{\mathrm{w}x}$ represents the total force exerted by the oblique wires along the horizontal direction while $F_{\mathrm{r}} \sin \beta$ is the horizontal component of the force provided by the external ropes, whose inclination angle is β (see Figure 2). It is noted that $\sin \beta = l_{\mathrm{d}} \sin \alpha / l_{\mathrm{r}}$, where l_{d} and l_{r} are the rod and rope lengths, respectively. In the undeformed configuration, the force in the oblique wires is zero while the forces arising in the rod and external ropes are equal but opposite. When the horizontal displacement of the cap is large enough, a force along the direction of motion (i.e., the negative stiffness) originates because β is small enough compared with α and, as a consequence, $F_{\mathrm{d}} \sin \alpha > \sum F_{\mathrm{w}x} + F_{\mathrm{r}} \sin \beta$ in Equation (1).

The proposed NSD is arranged in parallel with viscoelastic supports and a top plate to complete the isolation system, as shown in Figure 3. There are several benefits related to the use of the proposed NSD for seismic isolation. First, the multidirectional negative stiffness significantly reduces acceleration and forces transmitted by the seismic motion to the superstructure regardless of the direction of the incoming earthquake. Furthermore, the use of dissipative elements (i.e., SMA wires and PU elastic spring) enhances the equivalent damping. The dynamic behavior can be tailored to fulfill the target requirements by adjusting the pretension level and

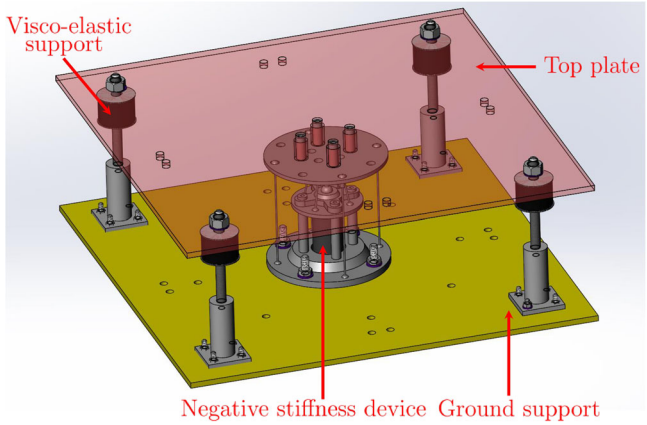

FIGURE 3 Three-dimensional virtual prototype model of the final isolation system based on the proposed negative-stiffness device.

the rod dimensions as well as the arrangement, number, size, and material of the wires. Further advantages related to the proposed device are its compact size and ease of installation.

3 | ANALYSIS OF THE NSD THROUGH A SEMIRECURSIVE METHOD

3.1 | Background

A multibody dynamics approach is established to simulate the response of the proposed NSD. A multibody system consists of multiple rigid bodies connected through a series of kinematic joints.[62] Specifically, the proposed NSD is a closed-loop multibody system. While the fully recursive method is an efficient approach to dealing with open-loop multibody systems, it cannot be directly applied to closed-loop multibody systems. A two-step semirecursive multibody dynamics method based on natural coordinates is thus proposed to extend the application of the original recursive approach to closed-loop multibody systems.[58,63] First, the closed-loop structure is opened by cutting kinematic joints, generating a tree topology. Afterward, the multibody dynamics equations in natural coordinates are established using the recursive method and mapped into the relative coordinates domain through the first velocity transformation. Hence, the dynamic equations of the closed-loop multibody system are derived by considering closed-loop constraint equations and introducing the second velocity transformation matrix, which is a basis for the null space of the closed-loop linearized constraint equations. This matrix transforms the dynamic equations from the relative coordinates domain to a set of mutually independent relative coordinates domains. Additionally, the second velocity transformation matrix eliminates the terms with Lagrange multipliers in the dynamic equations, reducing their complexity and improving the computational efficiency.

In the context of multibody dynamics, the geometric structure of bodies and their connectivity with neighboring bodies are described by natural coordinates defining a set of points and unit vectors in the moving body reference frame.[64] This geometric information can be easily expressed in global coordinates according to the types of joints between adjacent components. To simplify the equations of motion of the multibody system, the origin of the moving body reference system is selected so as to coincide instantaneously with the origin of the inertial reference system.[56,58]

Cartesian velocities $\boldsymbol{Z}$ and accelerations $\dot{\boldsymbol{Z}}$ of the multibody system are defined as follows:

$$\boldsymbol{Z}_i = \begin{bmatrix} \dot{\boldsymbol{s}}_i \\ \boldsymbol{\omega}_i \end{bmatrix}, \quad \dot{\boldsymbol{Z}}_i = \begin{bmatrix} \ddot{\boldsymbol{s}}_i \\ \dot{\boldsymbol{\omega}}_i \end{bmatrix}, \tag{2}$$

$$\boldsymbol{Z}^{\top} = \left\{ \boldsymbol{Z}_1^{\top} \;\; \boldsymbol{Z}_2^{\top} \;\; \cdots \;\; \boldsymbol{Z}_n^{\top} \right\}, \;\; \dot{\boldsymbol{Z}}^{\top} = \left\{ \dot{\boldsymbol{Z}}_1^{\top} \;\; \dot{\boldsymbol{Z}}_2^{\top} \;\; \cdots \;\; \dot{\boldsymbol{Z}}_n^{\top} \right\}, \tag{3}$$

where $\dot{\boldsymbol{s}}_i$ and $\ddot{\boldsymbol{s}}_i$ are the velocity and acceleration vectors of the origin of the ith body reference frame, respectively, with $i = 1, 2, \ldots, n$. Moreover, $\boldsymbol{\omega}_i$ and $\dot{\boldsymbol{\omega}}_i$ represent the angular velocity and angular acceleration vectors of the ith body, respectively. Herein, n denotes the number of bodies (excluding the fixed body).

Using a recursive approach, these kinematic descriptors in Cartesian coordinates are then mapped into the relative (joint) coordinates $\boldsymbol{z}$[58]:

$$\boldsymbol{Z} = \boldsymbol{R}_1 \dot{\boldsymbol{z}}_1 + \boldsymbol{R}_2 \dot{\boldsymbol{z}}_2 + \cdots + \boldsymbol{R}_n \dot{\boldsymbol{z}}_n = \boldsymbol{R}\dot{\boldsymbol{z}} = \boldsymbol{T}\boldsymbol{R}_{\mathrm{d}}\dot{\boldsymbol{z}}, \tag{4}$$

$$\dot{\boldsymbol{Z}} = \boldsymbol{T}\boldsymbol{R}_{\mathrm{d}}\ddot{\boldsymbol{z}} + \boldsymbol{T}\dot{\boldsymbol{R}}_{\mathrm{d}}\dot{\boldsymbol{z}}, \tag{5}$$

where the matrix $\boldsymbol{R}$ is the first velocity transformation matrix, which can be decomposed into the path matrix $\boldsymbol{T}$ and the diagonal matrix $\boldsymbol{R}_{\mathrm{d}}$. The path matrix $\boldsymbol{T}$, consisting of the identity matrix $\boldsymbol{I}$ and the zero matrix $\boldsymbol{0}$, reflects the topological relations among the bodies. Each element in the main diagonal of the matrix $\boldsymbol{R}_{\mathrm{d}}$ is calculated according to the type of the corresponding mechanical joint.

The equation of motion of the multibody system is obtained using the principle of virtual work. For an open-loop multibody system, the virtual power of internal forces and torques, including inertia forces, must be equal to the virtual power of the external forces. For a closed-loop system, the virtual power generated by constraint forces must be also taken into account. By introducing the first velocity transformation as per Equations (4) and (5), one obtains

$$\begin{aligned} \delta \boldsymbol{P} &= \left(\sum_{i=1}^{n} \delta \boldsymbol{Z}_i^{\top} \left(\overline{\boldsymbol{M}}_i \dot{\boldsymbol{Z}}_i - \overline{\boldsymbol{Q}}_i \right) \right) - \delta \dot{\boldsymbol{z}}^{\top} \boldsymbol{\Phi}_{\boldsymbol{z}}^{\top} \boldsymbol{\lambda} \\ &= \delta \dot{\boldsymbol{z}}^{\top} \left[\boldsymbol{R}_{\mathrm{d}}^{\top} \boldsymbol{M}^{\Sigma} \boldsymbol{R}_{\mathrm{d}} \ddot{\boldsymbol{z}} + \boldsymbol{R}_{\mathrm{d}}^{\top} \boldsymbol{M}^{\Sigma} \dot{\boldsymbol{R}}_{\mathrm{d}} \dot{\boldsymbol{z}} - \boldsymbol{R}_{\mathrm{d}}^{\top} \boldsymbol{Q}^{\Sigma} - \boldsymbol{\Phi}_{\boldsymbol{z}}^{\top} \boldsymbol{\lambda} \right] = 0, \end{aligned} \tag{6}$$

where $\overline{\boldsymbol{M}}_i$ and $\overline{\boldsymbol{Q}}_i$ represent the inertia matrix and the force vector, respectively, of the ith body. Moreover, $-\boldsymbol{\Phi}_{\boldsymbol{z}}^{\top}\boldsymbol{\lambda}$ is the vector of constraint forces related to the joint having coordinates $\boldsymbol{z}$. It accounts for the Jacobian matrix $\boldsymbol{\Phi}_{\boldsymbol{z}}$ of the closed-loop constraint equations $\boldsymbol{\Phi}$ along with the Lagrange multipliers vector $\boldsymbol{\lambda}$. Finally, $\boldsymbol{M}^{\Sigma}$ and $\boldsymbol{Q}^{\Sigma}$ denote the composite inertia matrices and the accumulated external

forces of the multibody system, respectively. They are calculated as follows:

$$\boldsymbol{M}^{\Sigma} = \boldsymbol{T}^{\top}\overline{\boldsymbol{M}}\,\boldsymbol{T}, \tag{7}$$

$$\boldsymbol{Q}^{\Sigma} = \boldsymbol{T}^{\top}\overline{\boldsymbol{Q}}, \tag{8}$$

where $\overline{\boldsymbol{M}} = \mathrm{diag}(\overline{\boldsymbol{M}}_1, \overline{\boldsymbol{M}}_2, ..., \overline{\boldsymbol{M}}_n)$ is the system inertia matrix whereas $\overline{\boldsymbol{Q}} = \left[\overline{\boldsymbol{Q}}_1^{\top} \;\; \overline{\boldsymbol{Q}}_2^{\top} \;\cdots\; \overline{\boldsymbol{Q}}_n^{\top}\right]^{\top}$ collects the external forces and torques acting on all bodies.

The relative velocity $\dot{\boldsymbol{z}}$ is divided into independent relative coordinates $\dot{\boldsymbol{z}}^{\mathrm{i}}$ and dependent relative coordinates $\dot{\boldsymbol{z}}^{\mathrm{d}}$. Similarly, the Jacobian matrix $\boldsymbol{\Phi}_{\boldsymbol{z}}$ can also be partitioned into an independent part denoted by $\boldsymbol{\Phi}_{\boldsymbol{z}}^{\mathrm{i}}$ and a dependent one denoted by $\boldsymbol{\Phi}_{\boldsymbol{z}}^{\mathrm{d}}$ through Gaussian elimination and matrix blocking. Hence, the following equality holds:

$$\left[\boldsymbol{\Phi}_{\boldsymbol{z}}^{\mathrm{d}}\boldsymbol{\Phi}_{\boldsymbol{z}}^{\mathrm{i}}\right]\begin{bmatrix}\dot{\boldsymbol{z}}^{\mathrm{d}}\\ \dot{\boldsymbol{z}}^{\mathrm{i}}\end{bmatrix} = \boldsymbol{\Phi}_{\boldsymbol{z}}^{\mathrm{d}}\dot{\boldsymbol{z}}^{\mathrm{d}} + \boldsymbol{\Phi}_{\boldsymbol{z}}^{\mathrm{i}}\dot{\boldsymbol{z}}^{\mathrm{i}} = \boldsymbol{0}. \tag{9}$$

The matrix $\boldsymbol{\Phi}_{\boldsymbol{z}}^{\mathrm{d}}$ is nonsingular because it contains the pivots of the Jacobian matrix. It implies that the relative velocity and acceleration can be expressed as follows:

$$\dot{\boldsymbol{z}} = \begin{bmatrix}-\left(\boldsymbol{\Phi}_{\boldsymbol{z}}^{\mathrm{d}}\right)^{-1}\boldsymbol{\Phi}_{\boldsymbol{z}}^{\mathrm{i}}\\ \boldsymbol{I}\end{bmatrix}\dot{\boldsymbol{z}}^{\mathrm{i}} = \boldsymbol{R}_{\boldsymbol{z}}\dot{\boldsymbol{z}}^{\mathrm{i}}, \tag{10}$$

$$\ddot{\boldsymbol{z}} = \boldsymbol{R}_{\boldsymbol{z}}\ddot{\boldsymbol{z}}^{\mathrm{i}} + \dot{\boldsymbol{R}}_{\boldsymbol{z}}\dot{\boldsymbol{z}}^{\mathrm{i}}, \tag{11}$$

where $\boldsymbol{R}_{\boldsymbol{z}}$ is the second velocity transformation matrix and provides the orthogonal complement of the Jacobian matrix $\boldsymbol{\Phi}_{\boldsymbol{z}}$ (i.e., its columns form the null space basis of $\boldsymbol{\Phi}_{\boldsymbol{z}}$). The Lagrange multiplier terms are thus eliminated by introducing $\boldsymbol{R}_{\boldsymbol{z}}$ into Equation (6). Since the virtual relative velocities are independent, the equations of motion for the proposed NSD considered as a closed-loop multibody system are expressed as[58,65,66]

$$\boldsymbol{R}_{\boldsymbol{z}}^{\top}\boldsymbol{R}_{\mathrm{d}}^{\top}\boldsymbol{M}^{\Sigma}\boldsymbol{R}_{\mathrm{d}}\boldsymbol{R}_{\boldsymbol{z}}\ddot{\boldsymbol{z}}^{\mathrm{i}} = \boldsymbol{R}_{\boldsymbol{z}}^{\top}\boldsymbol{R}_{\mathrm{d}}^{\top}\left[\boldsymbol{Q}^{\Sigma} - \boldsymbol{M}^{\Sigma}\frac{\mathrm{d}(\boldsymbol{R}_{\mathrm{d}}\boldsymbol{R}_{\boldsymbol{z}})}{\mathrm{d}t}\dot{\boldsymbol{z}}^{\mathrm{i}}\right]. \tag{12}$$

3.2 | Numerical modeling of the device

The tree topology of the proposed NSD must be defined to simulate its behavior through the semirecursive method. Figure 4 shows the spinning tree topology of the NSD, illustrating the connections and the recursive relationships among the various components within the dynamical system. The bodies of the system are connected through mechanical joints. For instance, the movable wall is connected to the low base through a one-degree-of-freedom (1-DOF) translational joint (z_7 in Figure 4) in the vertical direction with respect to the base. Multidegree-of-freedom joints, such as spherical joints, Hooke joints, and planar joints, are decomposed into combinations of translational and rotational joints by introducing some massless auxiliary bodies.

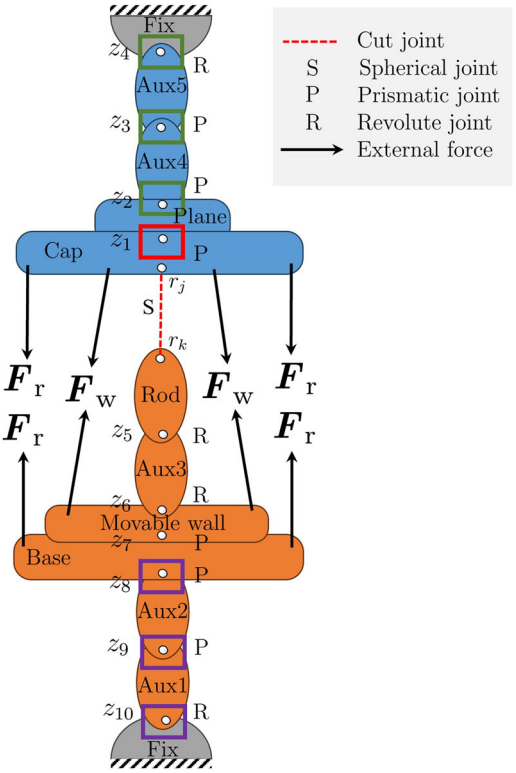

FIGURE 4 Tree topology for the multibody negative-stiffness device.

For example, the planar joint connecting the base to the fixed body (e.g., the ground) can be decomposed into a combination of two translational joints (z_8 and z_9 in Figure 4) moving in the X/Y directions, a rotational joint (z_{10} in Figure 4) rotating around the Z-axis, and two massless auxiliary bodies (Aux1 and Aux2 in Figure 4).

By prioritizing the trimming of high-degree-of-freedom joints to open closed structures,[63] the spherical joint between the cap and the rod is cut first. As a result, the closed-loop system is opened to form two branches that are recursively traced from the fixed body. By cutting the spherical joint, the loop-closure opening constrained equations are obtained as follows:

$$\boldsymbol{\Phi} = \boldsymbol{r}_j - \boldsymbol{r}_k = \boldsymbol{0}, \tag{13}$$

where $\boldsymbol{r}_j$ and $\boldsymbol{r}_k$ represent the position vector of the node on the cap and the rod, respectively. The Jacobian matrix for the constraint equation can be obtained using the chain rule:

$$\boldsymbol{\Phi}_{\boldsymbol{z}} = \frac{\partial \dot{\boldsymbol{r}}_j}{\partial \dot{\boldsymbol{z}}} - \frac{\partial \dot{\boldsymbol{r}}_k}{\partial \dot{\boldsymbol{z}}}. \tag{14}$$

As shown in Figure 4, the NSD consists of 11 bodies, including five virtual auxiliary bodies and 10 1-DOF joints. The Cartesian velocities $\boldsymbol{Z}$ and accelerations $\dot{\boldsymbol{Z}}$ of the device can be described by Equations (2) and (3) with $n = 10$. They are further converted into relative coordinates $\boldsymbol{z}$ by introducing the first velocity transformation

according to Equations (4) and (5). The path matrix $\boldsymbol{T}$ can be directly retrieved from the topological relationships among the bodies, thus obtaining

$$\boldsymbol{T} = \begin{bmatrix} \boldsymbol{I} & \boldsymbol{I} & \boldsymbol{I} & \boldsymbol{I} & \boldsymbol{0} & \boldsymbol{0} & \boldsymbol{0} & \boldsymbol{0} & \boldsymbol{0} & \boldsymbol{0} \\ \boldsymbol{0} & \boldsymbol{I} & \boldsymbol{I} & \boldsymbol{I} & \boldsymbol{0} & \boldsymbol{0} & \boldsymbol{0} & \boldsymbol{0} & \boldsymbol{0} & \boldsymbol{0} \\ \boldsymbol{0} & \boldsymbol{0} & \boldsymbol{I} & \boldsymbol{I} & \boldsymbol{0} & \boldsymbol{0} & \boldsymbol{0} & \boldsymbol{0} & \boldsymbol{0} & \boldsymbol{0} \\ \boldsymbol{0} & \boldsymbol{0} & \boldsymbol{0} & \boldsymbol{I} & \boldsymbol{0} & \boldsymbol{0} & \boldsymbol{0} & \boldsymbol{0} & \boldsymbol{0} & \boldsymbol{0} \\ \boldsymbol{0} & \boldsymbol{0} & \boldsymbol{0} & \boldsymbol{0} & \boldsymbol{I} & \boldsymbol{I} & \boldsymbol{I} & \boldsymbol{I} & \boldsymbol{I} & \boldsymbol{I} \\ \boldsymbol{0} & \boldsymbol{0} & \boldsymbol{0} & \boldsymbol{0} & \boldsymbol{0} & \boldsymbol{I} & \boldsymbol{I} & \boldsymbol{I} & \boldsymbol{I} & \boldsymbol{I} \\ \boldsymbol{0} & \boldsymbol{0} & \boldsymbol{0} & \boldsymbol{0} & \boldsymbol{0} & \boldsymbol{0} & \boldsymbol{I} & \boldsymbol{I} & \boldsymbol{I} & \boldsymbol{I} \\ \boldsymbol{0} & \boldsymbol{0} & \boldsymbol{0} & \boldsymbol{0} & \boldsymbol{0} & \boldsymbol{0} & \boldsymbol{0} & \boldsymbol{I} & \boldsymbol{I} & \boldsymbol{I} \\ \boldsymbol{0} & \boldsymbol{0} & \boldsymbol{0} & \boldsymbol{0} & \boldsymbol{0} & \boldsymbol{0} & \boldsymbol{0} & \boldsymbol{0} & \boldsymbol{I} & \boldsymbol{I} \\ \boldsymbol{0} & \boldsymbol{0} & \boldsymbol{0} & \boldsymbol{0} & \boldsymbol{0} & \boldsymbol{0} & \boldsymbol{0} & \boldsymbol{0} & \boldsymbol{0} & \boldsymbol{I} \end{bmatrix}. \tag{15}$$

The joint coordinates are divided into independent relative coordinates $\boldsymbol{z}^{\mathrm{i}}$ and dependent relative coordinates $\boldsymbol{z}^{\mathrm{d}}$, as shown in Table 1. Force–displacement hysteresis cycles in the parametric analysis are obtained by assuming that the base is fixed (joint coordinates in the purple box in Figure 4) while applying a drive to the cap (green box in Figure 4). It is noted that the system has only 1-DOF (red box in Figure 4).

The external force vector $\overline{\boldsymbol{Q}}$ in Equation (8) includes the tension force generated by the rope $\boldsymbol{F}_{\mathrm{r}}$, the pulling force $\boldsymbol{F}_{\mathrm{w}}$ due to the stretching deformation of the oblique wire, and the elastic force $\boldsymbol{F}_{\mathrm{s}}$ produced by the elastic spring acting on the movable wall and the base. Since the ropes of the proposed NSD are made of high-strength material, it is assumed that they do not exceed the elastic deformation limit state throughout the entire deformation process. Hence, $\boldsymbol{F}_{\mathrm{r}}$ is expressed as follows:

$$\boldsymbol{F}_{\mathrm{r}} = k_{\mathrm{r}}(l_{\mathrm{r}} - l_{\mathrm{r},0})H(l_{\mathrm{r}} - l_{\mathrm{r},0})\boldsymbol{u}_{\mathrm{r}}, \tag{16}$$

where k_{r} represents the stiffness of the ropes whereas l_{r} and $l_{\mathrm{r},0}$ denote the current and original (i.e., before pretensioning) length of the ropes, respectively. The symbol $H(\cdot)$ is the Heaviside step function, and $\boldsymbol{u}_{\mathrm{r}}$ indicates the unit vector along the rope axis. The wires are made of SMA and their behavior is simulated by the rate-independent model proposed by Charalampakis and Tsiatas.[67] Consequently, $\boldsymbol{F}_{\mathrm{w}}$ is determined as[60]

$$\boldsymbol{F}_{\mathrm{w}} = \sigma_{\mathrm{w}} A_{\mathrm{w}} H(\sigma_{\mathrm{w}})\boldsymbol{u}_{\mathrm{w}}, \tag{17a}$$

$$\sigma_{\mathrm{w}} = (1 - s(\varepsilon_{\mathrm{w}}))E\left[\dot{\varepsilon}_{\mathrm{w}} - |\dot{\varepsilon}_{\mathrm{w}}|\mathrm{sgn}(\sigma_{\mathrm{w}} - \beta_{\mathrm{w}})\left(\frac{|\sigma_{\mathrm{w}} - \beta_{\mathrm{w}}|}{Y}\right)^{\eta_{\mathrm{w}}}\right] + s(\varepsilon_{\mathrm{w}})E_{\mathrm{m}}\dot{\varepsilon}_{\mathrm{w}}, \tag{17b}$$

$$\beta_{\mathrm{w}} = E\alpha_{\mathrm{w}}\left[\varepsilon_{\mathrm{w}} - \frac{\sigma_{\mathrm{w}}}{E} + f_{\mathrm{T}}\tanh(a\varepsilon_{\mathrm{w}})H(-\varepsilon_{\mathrm{w}}\dot{\varepsilon}_{\mathrm{w}})\right], \tag{17c}$$

$$s(\varepsilon_{\mathrm{w}}) = \frac{\tanh(c(|\varepsilon_{\mathrm{w}}| - \varepsilon_{\mathrm{t}})) + 1}{2}, \tag{17d}$$

where σ_{w} and ε_{w} are the stress and strain of the wires, respectively, whereas A_{w} is the cross-sectional area of the wire, and $\boldsymbol{u}_{\mathrm{w}}$ represents the unit vector along the wire axis. Moreover, E is the initial Young modulus during the austenitic phase, Y is the yielding stress, α_{w} is the parameter controlling the postelastic slope of the curve, and η_{w} rules the smoothness of the transition from the elastic to the postelastic range. Moreover, f_{T} controls the twinning hysteresis and superelasticity, whereas a defines the pinching around the origin along the cycle. Finally, E_{m} is the modulus during the fully martensitic phase, ε_{t} is the displacement at which the transition from the postelastic to the fully martensitic phase occurs, and c controls the smoothness of this transition. The response of the spring is described by the following Bouc–Wen model[68]:

$$\boldsymbol{F}_{\mathrm{s}} = (k_{\mathrm{s,e}}x_{\mathrm{s}} + \zeta)\boldsymbol{u}_{\mathrm{s}}, \tag{18a}$$

$$\dot{\zeta} = [k_{\mathrm{s,d}} - (\gamma_{\mathrm{s}} + \beta_{\mathrm{s}}\,\mathrm{sgn}(\zeta\,\dot{x}_{\mathrm{s}}))|\zeta|^{\eta_{\mathrm{s}}}]\dot{x}_{\mathrm{s}}, \tag{18b}$$

where x_{s} represents the deformation of the spring and $\boldsymbol{u}_{\mathrm{s}}$ is the unit vector denoting the direction of the restoring force. Moreover, $k_{\mathrm{s,e}}$ is the elastic stiffness, whereas $k_{\mathrm{s,d}}$, β_{s}, γ_{s}, and η_{s} rule the shape of the hysteresis loops.

4 | NUMERICAL INVESTIGATIONS

4.1 | Geometrical and mechanical data

Table 2 provides an overview of the general data related to the NSD geometry and mass properties. As far as the constitutive modeling of the NSD components is concerned, the ropes are described by a nonlinear piecewise function that generates no force during contraction while it follows Hooke's law during extension. The rope stiffness k_{r} in Equation (16) is set to 500 kN/m. The nonlinear mechanical parameters for the wires and the spring are given in Tables 3 and 4, respectively.

4.2 | Results

The analysis of the proposed NSD through the semirecursive multibody dynamics approach was performed by solving Equation (12)

TABLE 1 Relative coordinates for the multibody analysis of the negative-stiffness device.

Numerical investigation	Independent coordinates z^{i}			Dependent coordinates z^{d}
	Drive coordinates	Free coordinates	Constrained coordinates	
Parametric analysis	z_2, z_3, z_4	z_1 (or z_7)	z_8, z_9, z_{10}	z_5, z_6
Dynamic simulation	z_8, z_9, z_{10}	z_1 (or z_7), z_2, z_3, z_4	–	z_5, z_6

TABLE 2 General data about the geometry of the negative-stiffness device.

Parameter	Description	Value
R_c	Diameter of the cap	0.128 m
m_c	Mass of the cap	0.737 kg
l_d	Length of the rod	0.030 m
m_d	Mass of the rod	0.017 kg
R_l	Diameter of the vertical movable wall	0.074 m
m_l	Mass of the vertical movable wall	0.210 kg
R_b	Diameter of the base	0.128 m
m_b	Mass of the base	1.082 kg
n_r	Number of the ropes	4
$R_{r,u}$	Radius of the circular pattern of the ropes' upper ends	0.055 m
$R_{r,l}$	Radius of the circular pattern of the ropes' lower ends	0.055 m
n_w	Number of the wires	4
D_w	Diameter of the wire cross-section	2 mm
$R_{w,u}$	Radius of the circular pattern of the wires' upper ends	0.0165 m
$R_{w,l}$	Radius of the circular pattern of the wires' lower ends	0.0265 m
δ_0	Angle between the first wire projection on the horizontal plane and X-axis	0°
θ	Inclination angle of the oblique wires	12.8°
l_s	Length of the spring after precompression	62 mm

TABLE 3 Mechanical parameters of the wires.

Parameter	Description	Value
E	Initial modulus during the austenitic phase	46823.455 MPa
Y	Yielding stress	314.844 MPa
E_m	Modulus during the fully martensitic phase	19291.59 MPa
η_w	Hysteresis shape parameter	1.327
α_w		0.148
f_T		0.064
a		194.224
c		99.135
ε_t		0.052

TABLE 4 Mechanical parameters of the spring.

Parameter	Description	Value
$k_{s,e}$	Elastic stiffness	0.35959 kN/mm
F_{press}	Precompression force	3800 N
$k_{s,d}$	Hysteresis shape parameter	0.249428 kN/mm
η_s		1.5
γ_s		1 kN$^{-\eta_s+1}$/mm
β_s		1.23 kN$^{-\eta_s+1}$/mm

with an in-house code implemented in MATLAB version 2023b. The corresponding set of ordinary differential equations is numerically solved using the Runge–Kutta–Fehlberg method (RKF45). At the same time, a reference dynamical model has been developed via the software ADAMS 2020 to assess the accuracy of the semirecursive multibody dynamics model. Figure 5 provides a 3D view of the NSD model developed in ADAMS 2020. It is to be noted that ropes, wires, and springs of the NSD are replaced by equivalent forces applied at their respective points (i.e., between two bodies in line-of-sight). The virtual plate is a massless auxiliary entity and is solely used to constrain the displacement of the cap. It is connected to the cap through a translational joint and linked to the ground via a planar joint (allowing movement in the XY plane and rotation around the Z-axis). All joints are treated as ideal smooth joints, and friction between components is neglected.

The force–displacement response of the NSD is obtained by imposing a sinusoidal displacement to the cap in the X-direction with assigned frequency f and amplitude A. Figure 6 illustrates the force–displacement cycles obtained through the implemented semirecursive method and by the model implemented in ADAMS. Results in Figure 6 are carried out for $A = \{0.015, 0.0255\}$ m and $f = \{1, 10\}$ Hz. The results obtained using the semirecursive method are highly consistent with those obtained by ADAMS. The difference is maximum when the NSD achieves the largest displacement, but the error is always negligible. The obtained agreement validates the numerical model of the NSD developed using the semirecursive method.

The analysis of the force–displacement response provides further insights into the working mechanism of the proposed NSD. Figure 7 demonstrates that the proposed device exhibits a positive stiffness for small displacements. This is due to the inclined wires in the NSD. The stiffness decreases significantly and achieves a nearly constant negative value for larger displacements. As the displacement further increases, the absolute value of the generated negative stiffness gradually reduces until a critical value is reached, and then the device switches back to a positive stiffness. In the positive-stiffness region, the NSD limits the maximum deformation of the controlled structure to ensure its stability. It is to be noted that the NSD fails when the displacement exceeds the working range.

4.3 | Parametric analysis

A numerical study is performed to investigate the influence of some parameters, namely, the rod length l_d, number of ropes n_r, rope

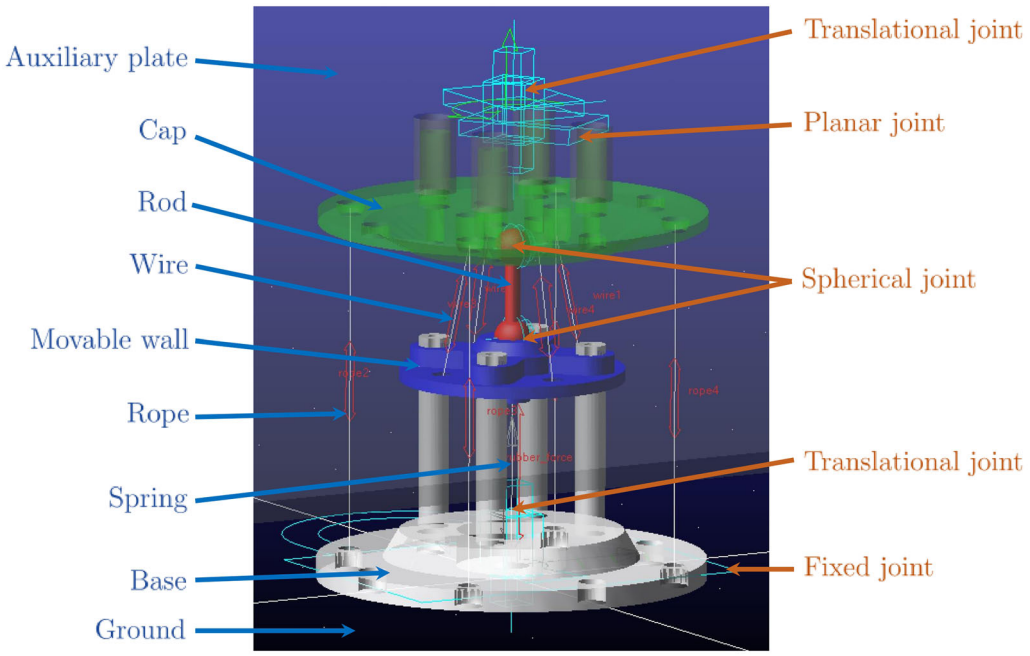

FIGURE 5 Three-dimensional view of the negative-stiffness device model developed in ADAMS 2020 (the device components are highlighted on the left, the mechanical joints are shown on the right).

stiffness k_r, precompression force F_{press}, wire diameter D_w, number of oblique wires n_w, and inclination angle θ of the oblique wires. For each individual parametric analysis, the numerical value of the parameter under consideration is changed while keeping the remaining parameters constant according to Tables 2–4. The force–displacement curves of the NSD for this parametric study are obtained by imposing an external sinusoidal displacement to the cap with assigned frequency f = 10 Hz and amplitude A = 0.024 m. The input direction corresponds to the positive direction of the X-axis, and it coincides with the projected line of the first wire (which can be pointed arbitrarily) on the horizontal plane. This numerical investigation facilitates the assessment of the influence of each individual parameter on the overall behavior and performance, providing useful directions for design optimization.

A rod length varying between 0.03 and 0.10 m with a constant step equal to 0.01 m is assumed. Results in Table 5 demonstrate that the rod length l_d has a large influence on the NSD's maximum horizontal displacement X_{max}. As the rod length l_d increases, the maximum horizontal displacement of the cap becomes larger, while the maximum rotational angle of the rod θ_{max} decreases. This implies that the use of longer rod components can expand the maximum working range of the NSD. Figure 8 illustrates the force–displacement curves of the NSD for different rod lengths within their respective working ranges. Figure 8 shows that as the length of the rod increases, both force and stiffness decrease. Nevertheless, the changes in force and stiffness exhibit a smoother trend, with the operating range in which the device displays negative stiffness gradually expanding. Furthermore, the length of the rod plays a critical role in the device's ability to withstand minor displacements near the initial equilibrium position. When l_d > 0.05 m, the initial stiffness of the device turns negative, signifying a decrease in its effectiveness in mitigating minor displacements. This is attributed to the increase in rod length, resulting in a reduction of the inclined angle of the wires. Specifically, the horizontal component of the force exerted by the oblique wire $\boldsymbol{F}_w$ gradually diminishes, proving inadequate to counterbalance the horizontal component of the thrust from the connecting rod. Consequently, the device loses its capacity to resist small displacements near the initial equilibrium position, leading to a negative-stiffness condition.

The number of external ropes for this parametric study is assumed to be between 3 and 9. Results in Figure 9 show that the number of ropes n_r mainly affects the trend of negative stiffness. The negative-stiffness range expands with a decrease in the number of external ropes. This phenomenon stems from the reduction in overall stiffness when the number of ropes is lowered. Consequently, the ropes generate a diminished horizontal component of the force $\boldsymbol{F}_r$ for the same cap displacement, thereby amplifying the total horizontal force on the cap and, in turn, increasing the negative stiffness.

A rope stiffness between 300 and 900 kN/m with constant increments of 200 kN/m is considered. As expected, the results in Figure 10 for different rope stiffnesses are consistent with the conclusions drawn about the influence of the rope number. The larger the rope stiffness, the lower the control force and the shorter the operating range in which the device exhibits negative stiffness. Notably, if k_r > 700 kN/m, then the hysteresis response no longer undergoes significant changes because the ropes' behavior becomes more similar to that of a rigid body.

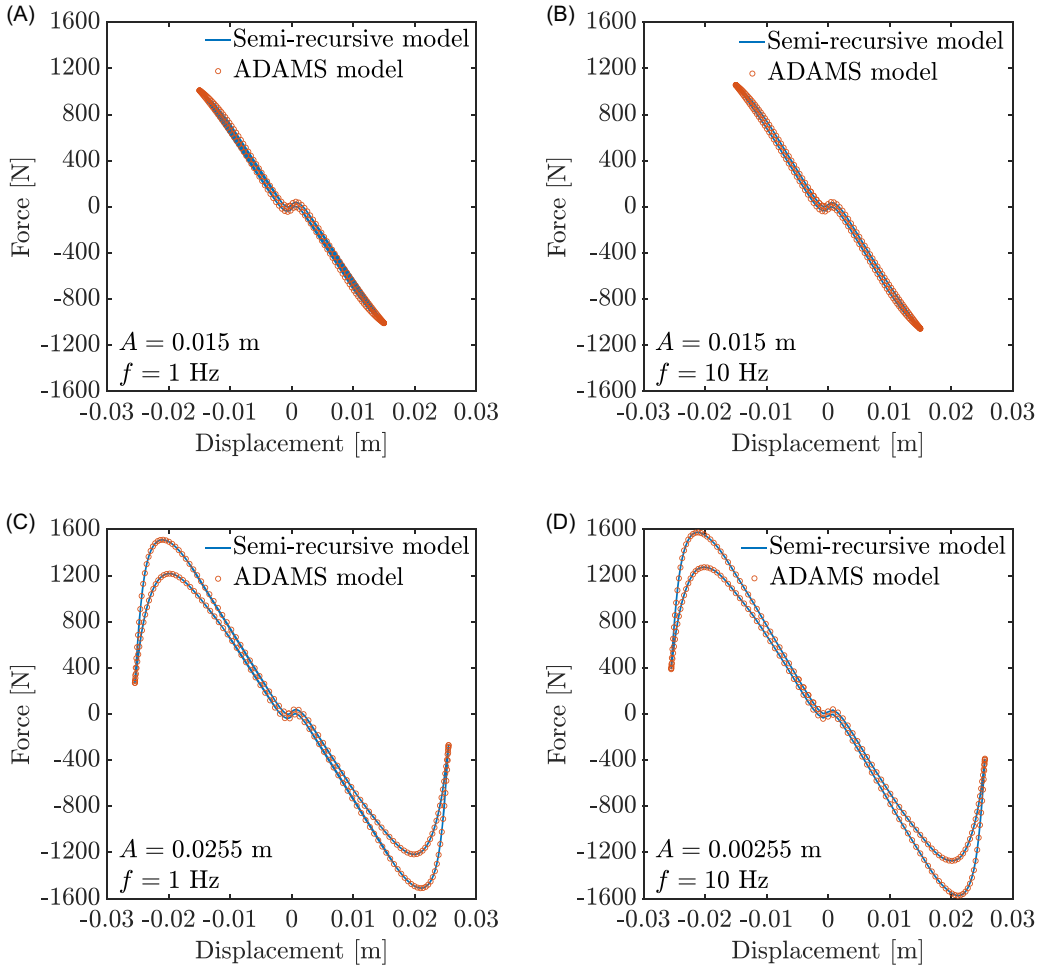

FIGURE 6 Force–displacement curves of the negative-stiffness device: (A) A = 0.015 m and f = 1 Hz, (B) A = 0.015 m and f = 10 Hz, (C) A = 0.0255 m and f = 1 Hz, and (D) A = 0.0255 m and f = 10 Hz.

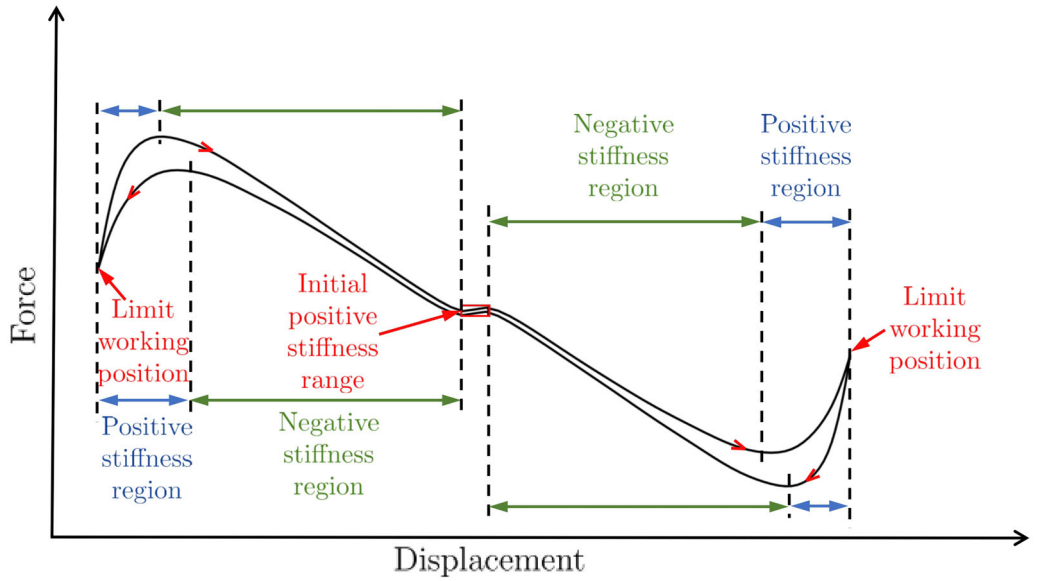

FIGURE 7 Identification of the main working regions in the force–displacement response of the negative-stiffness device.

TABLE 5 Maximum horizontal displacement of the negative-stiffness device and maximum rotation of the rod for different rod lengths.

l_d (m)	0.03	0.04	0.05	0.06	0.07	0.08	0.09	0.10
X_{max} (m)	±0.0255	±0.0315	±0.0372	±0.0427	±0.0481	±0.0533	±0.0585	±0.0635
θ_{max} (°)	58.21	52.04	48.14	45.40	43.37	41.79	40.51	39.44

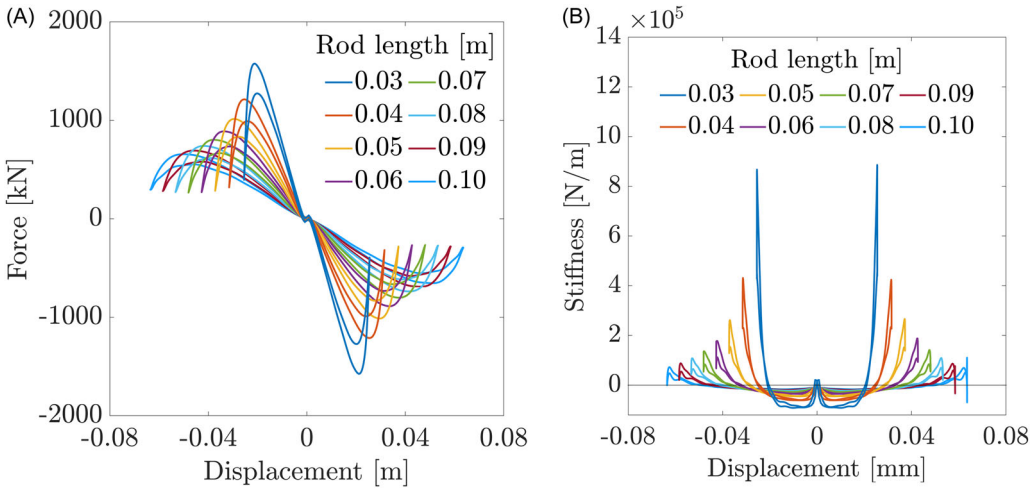

FIGURE 8 Influence of the rod length on (A) the force–displacement cycles and (B) the tangent stiffness-displacement cycles of the negative-stiffness device.

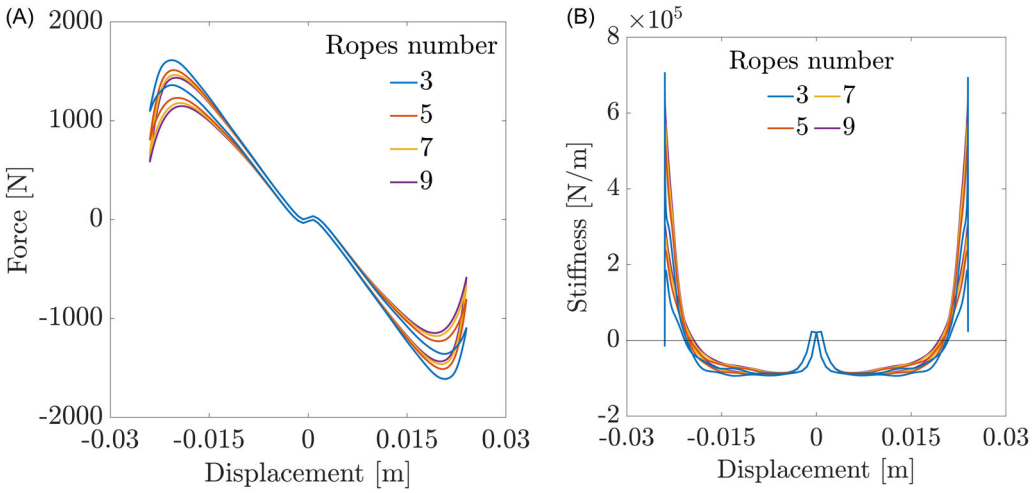

FIGURE 9 Influence of the ropes number on (A) the force–displacement cycles and (B) the tangent stiffness-displacement cycles of the negative-stiffness device.

The maximum precompression force F_{press} that the spring can withstand depends on both its material and geometry. The parametric study for F_{press} has been performed considering evenly spaced values between 2400 and 3800 N with constant increments of 200 kN. The results in Table 6 confirm that this parameter significantly affects the displacement capacity of the device. Particularly, the larger the F_{press}, the wider the working range of the device. However, such increment of the working range becomes progressively less apparent for larger and larger values of F_{press}. Results for a maximum precompression force F_{press} between 2400 and 3600 N with constant steps of 400 N are shown in Figure 11. They also highlight that low values of F_{press} result in a reduced control force generated by the NSD and flatten the hysteresis cycles. It is also evident that, although the increment of the precompression force reduces the stiffness against small displacements, it effectively widens the operating range in which the device exhibits negative stiffness.

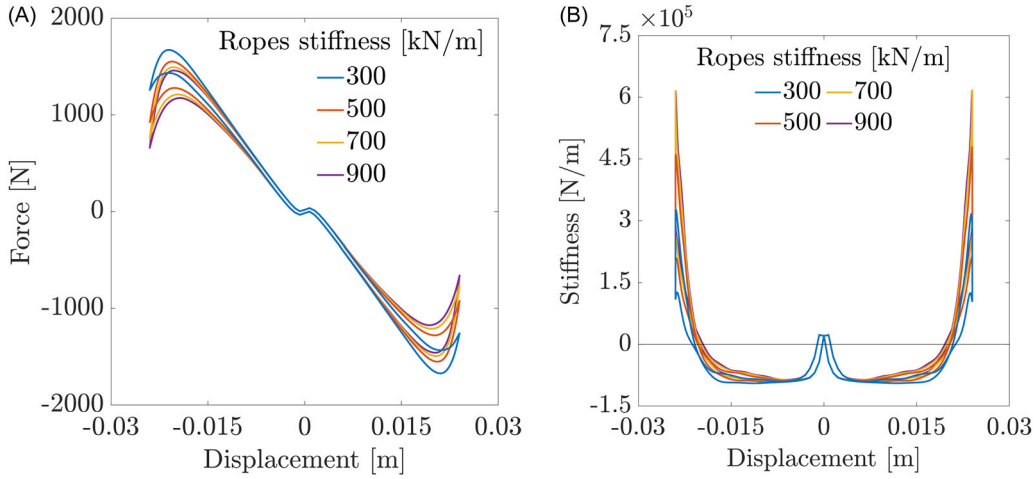

FIGURE 10 Influence of rope stiffness on (A) the force–displacement cycles and (B) the tangent stiffness-displacement cycles of the negative-stiffness device.

TABLE 6 Maximum horizontal displacement of the negative-stiffness device for different values of the precompression force.

F_{press} (N)	2400	2600	2800	3000	3200	3400	3600	3800
X_{max} (m)	±0.0208	±0.0216	±0.0224	±0.0231	±0.0238	±0.0244	±0.0249	±0.0255

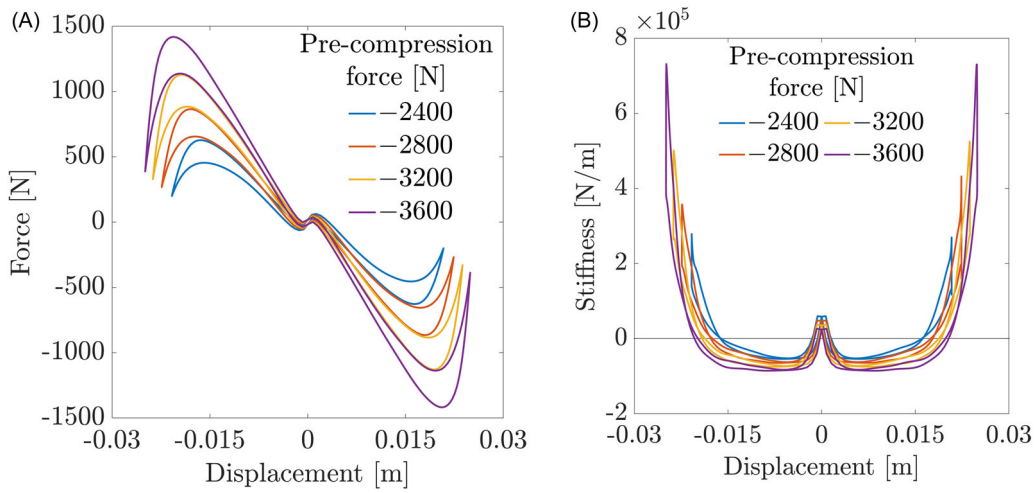

FIGURE 11 Influence of the precompression force on (A) the force–displacement cycles and (B) the tangent stiffness-displacement cycles of the negative-stiffness device.

The influence of the wire cross-section diameter D_w is investigated between 1.2 and 2.4 mm. This is a critical parameter that rules the behavior of the NSD at small displacements near the initial equilibrium position. Figure 12 illustrates the impact of D_w on the response of the NSD. As expected, thicker wires are more effective in resisting small displacements near the initial equilibrium position. Thicker wires also entail a larger area enclosed by the hysteresis loop, as shown in Figure 13, highlighting a beneficial increment of dissipated energy. This effect arises from the fact that the wires are made of SMA, and its internal phase transformations introduce a dissipative behavior in the working mechanism of the NSD. This implies that increasing the wire thickness amplifies the equivalent damping of the device.

Figure 14 quantifies the influence of the wire number on the performance of the NSD. Herein, the number of wires n_w between 3 and 10 is considered. These plots demonstrate that increasing the number of oblique wires can enhance the positive stiffness within the initial small displacement range. However, this simultaneously disrupts

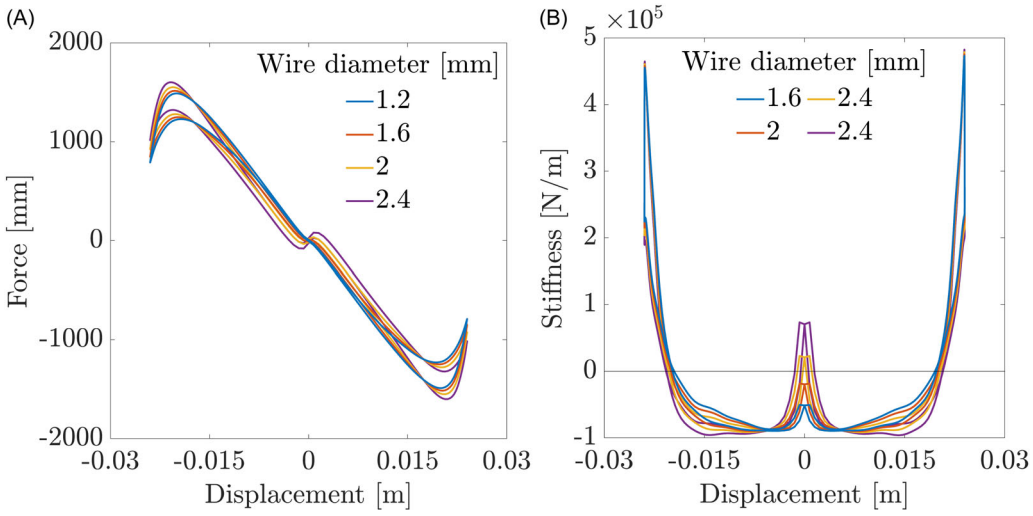

FIGURE 12 Influence of the wire cross-section diameter on (A) the force–displacement cycles and (B) the tangent stiffness-displacement cycles of the negative-stiffness device.

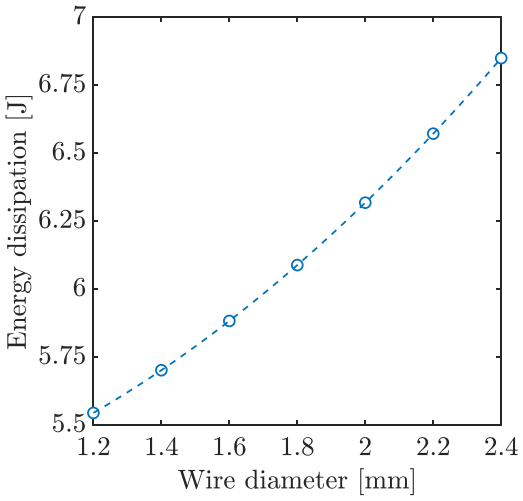

FIGURE 13 Effect of the wire cross-section diameter on the energy dissipation of the negative-stiffness device.

the symmetry of the resulting stiffness. When n_w is an odd number, the asymmetry of the wires relative to the *Y*-axis results in a sudden change in the negative-stiffness region on one side of the cycle. Due to the topological relationship among cap, rod, and movable wall, there exists a nonlinear relationship between wire elongation and cap displacement. Figure 15 shows that a wire plays a primary role when the angle δ between its horizontal projection and the deformation direction of the NSD is either 0° or 180° while it vanishes for δ approaching either 90° or 270°. Figure 16 illustrates the influence of the horizontal force of the wire on the force–displacement curves of the NSD and explains the occurrence of sudden changes in the hysteresis loop within the negative-stiffness region.

Finally, the role of the wire inclination angle θ between 0° and 22.4° is investigated in Figures 17 and 18. Figure 18 illustrates the influence of the wire inclination angle θ on the elongation of the first wire (horizontal projection along the deformation direction). Figure 18 confirms that the wire does not stretch when the inclination angle is zero (i.e., vertical wire). In this case, the control force curve pinches at the origin, that is, there is no stabilizing force generated by the NSD near the initial equilibrium position, and the corresponding tangent stiffness curve is negligible. On the one hand, for small wire inclinations, it can be inferred from Figure 19 that the wire force goes to zero for θ = 0° or 3.2° when point *a* is exceeded. Once point *b* is overcome, the wires are ineffective for θ = 0°, 3.2°, and 6.4°. On the other hand, Figure 19 also illustrates the influence of large wire inclinations on the force–displacement hysteresis cycles. Herein, it is evident that a large wire inclination is beneficial to resist small perturbations, but this can reduce the control effectiveness and the device's stability. Figure 20 shows that increasing the wire inclination angle from θ = 6.4° to 16° significantly enhances the energy dissipation capacity of the NSD. On the other hand, modest improvements are obtained for θ > 16°.

4.4 | Guidelines for design optimization

The parametric analysis allows us to guide the design optimization of the seismic isolation system based on the proposed NSD. The following primary highlights can be sketched.

- The rod length as well as the diameter, number, and inclination angle of the wires have a significant impact on the initial stiffness. It is recommended to assume the number of wires equal to 4 or 8, as multiples of 4 wires ensure axial symmetry relative to both *X*- and *Y*-axes, thereby expanding the stable operating range of the device. A wire inclination angle ranging between 9.6° and 16° is suggested to ensure that the wires remain effective and do not undergo plastic deformations. Additionally, the wire cross-section

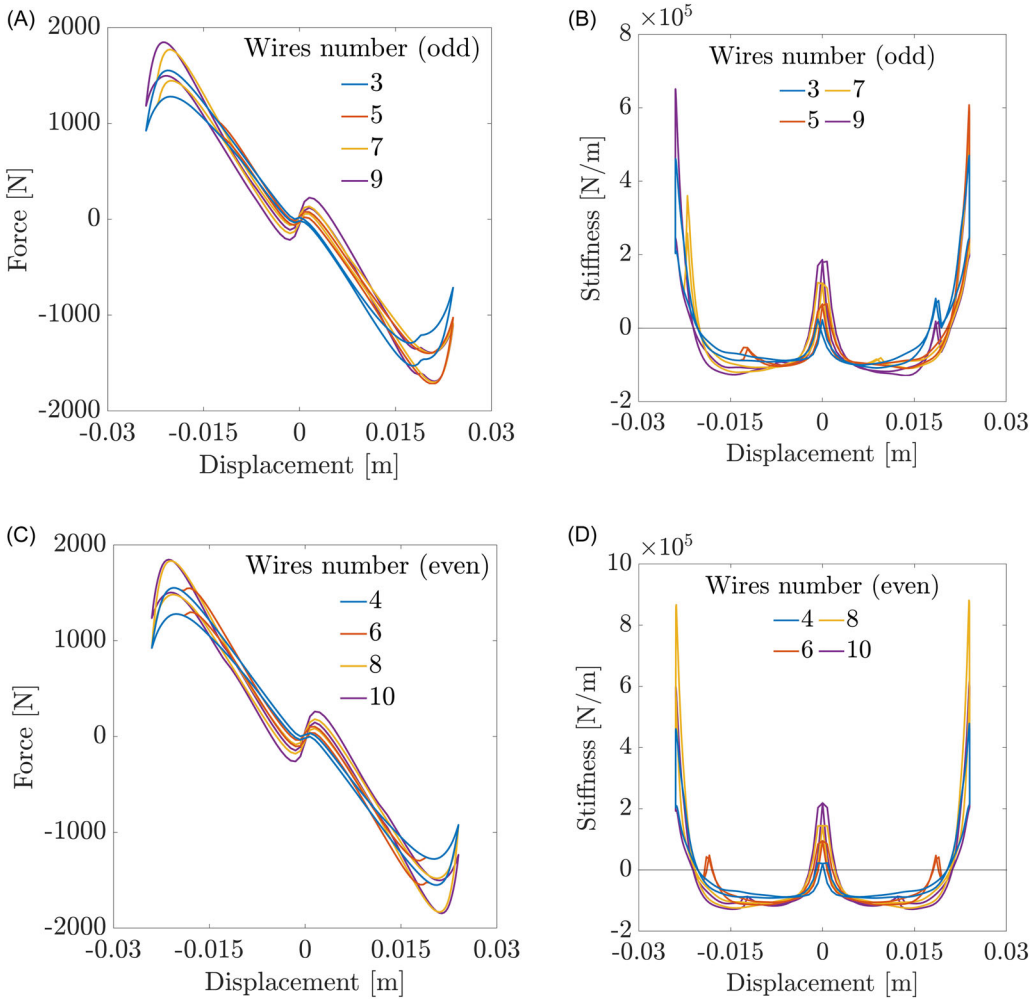

FIGURE 14 Influence of the number of the wires on (A, C) the force–displacement cycles and (B, D) the tangent stiffness-displacement cycles of the negative-stiffness device.

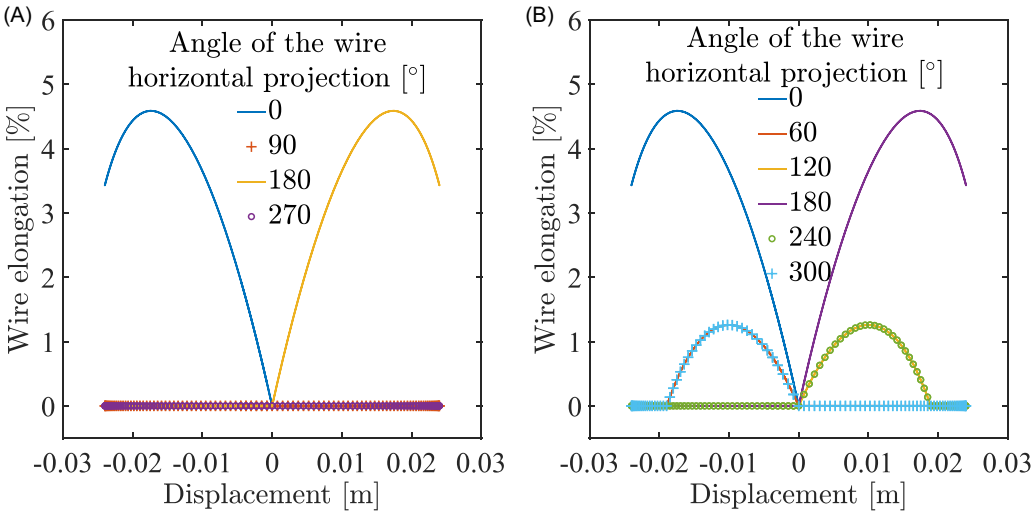

FIGURE 15 Relationship between wire elongation and displacement for the number of wires equal to (A) 4 and (B) 6.

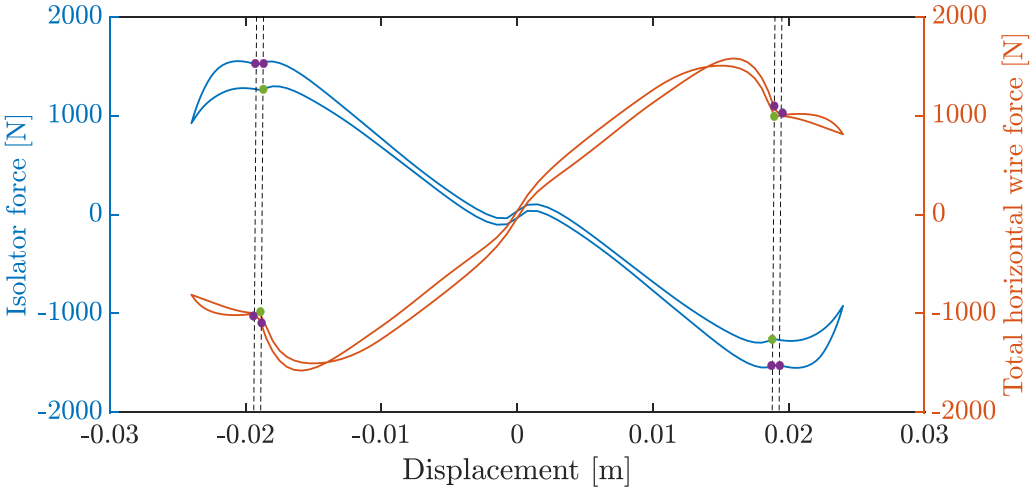

FIGURE 16 Effect of the total wires' horizontal force on the hysteretic response for the number of wires equal to 6.

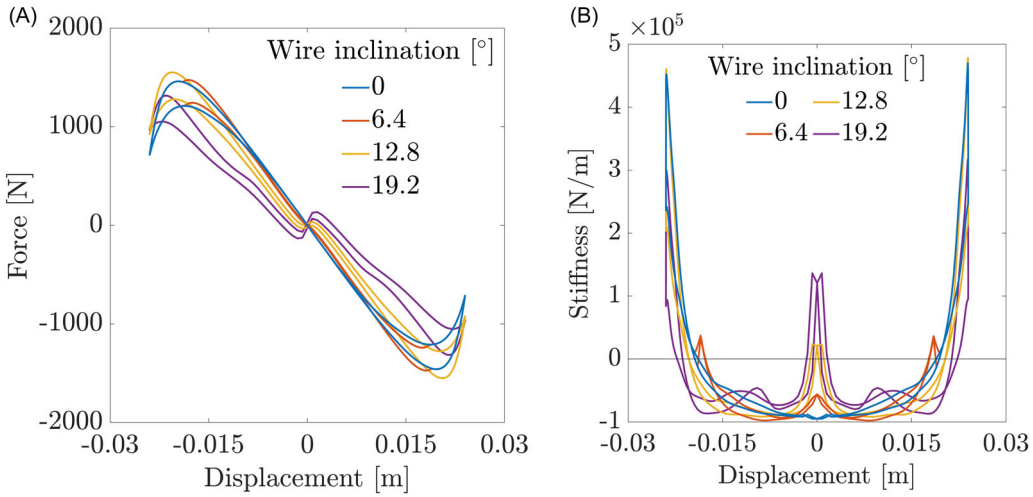

FIGURE 17 Influence of the wire inclination angle on (A) the force–displacement cycles and (B) the tangent stiffness-displacement cycles of the negative-stiffness device.

diameter can be adjusted to control the amount of wires' force, in such a way as to regulate the NSD's initial stiffness for small displacements.

- The rod length and precompression force are the main design parameters affecting the width of NSD's negative-stiffness range. For the same rotation angle of the rod, a longer rod length results in a larger horizontal displacement at the end connected to the cap, thereby extending the operating range. A higher precompression force also widens the operating range where the device exhibits negative stiffness by expanding the spring's elastic range.
- The number and stiffness of the ropes are secondary design parameters that can be properly tuned to rule the variation of the NSD's negative stiffness. A moderate reduction of their value is recommended to attain a broader operating range in which the device exhibits negative stiffness. In fact, according to a kinematic analysis, this allows the spring to remain in the elastic range.
- The rod length and precompression force play a pivotal role in shaping the control force magnitude and influencing the amplitude of the NSD's operating range. For an assigned displacement at the top cap, the length of the rod determines its rotational angle. This, in turn, influences the horizontal force exerted on the cap, thereby determining the magnitude of the negative stiffness.

5 | CONCLUSIONS

In this study, a novel NSD designed for seismic protection has been discussed. The focus was placed on the conceptualization, numerical modeling, and assessment of the proposed NSD. A numerical model was developed using a two-step semirecursive method to compute the nonlinear force–displacement relationship of the device. Initial validation involved comparing the model's results with those obtained using

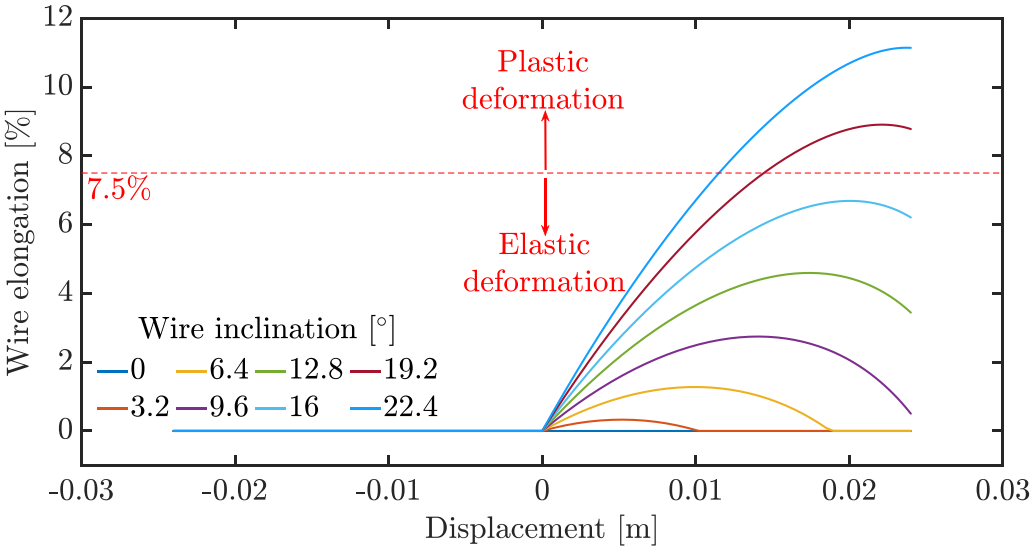

FIGURE 18 Effect of the wire inclination angle on their elongation (considering an angle between the horizontal projection of the wire and the deformation direction of the device equal to zero).

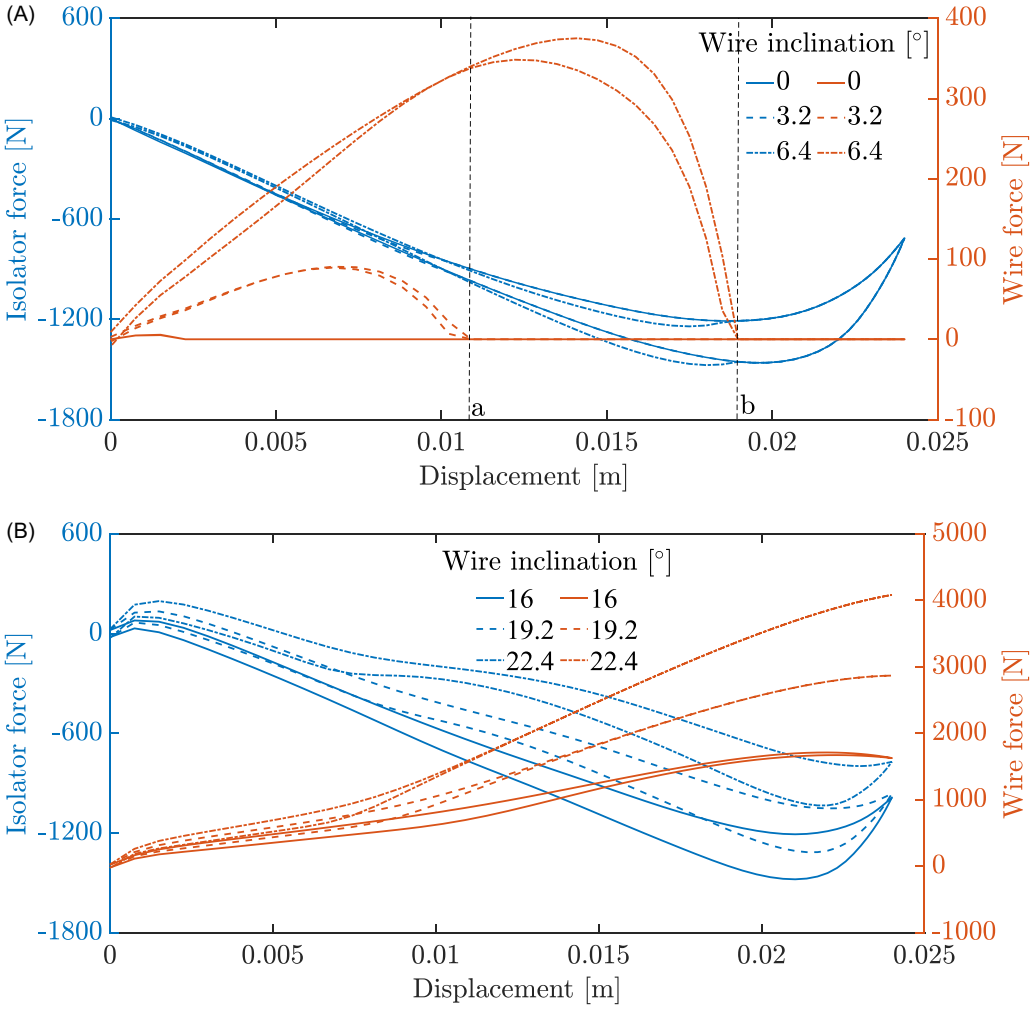

FIGURE 19 Variation of the hysteretic response for (A) small and (B) large wires' inclination angles.

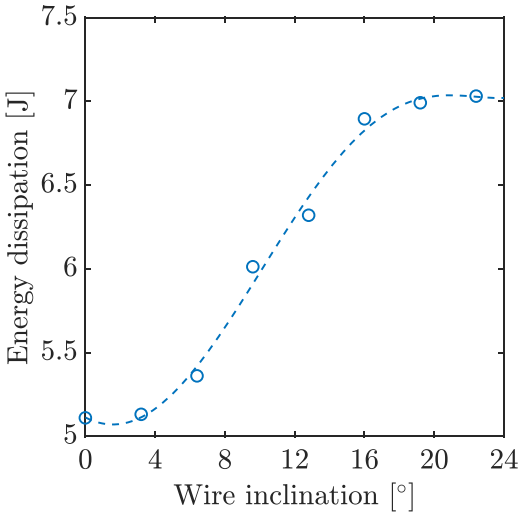

FIGURE 20 Effect of the wire inclination angle on the dissipated energy.

the commercial software ADAMS. Subsequent to validation, a comprehensive parametric analysis was conducted.

Key findings from the analysis include the significant influence of wire number, diameter, initial inclination, and connecting rod length on the device's initial stiffness. Notably, adjusting the wire diameter emerged as the most effective means of tuning the initial stiffness. The number and stiffness of ropes had minimal impact on the stiffness near the initial position and marginal influence on the negative-stiffness range. Conversely, the connecting rod length and spring precompression force exhibited a substantial influence on the range where negative stiffness is generated. Longer connecting rods or higher initial spring compression forces can expand the device's ultimate working range, although this comes with the trade-off of reduced control force.

Ongoing efforts involve the fabrication and experimental testing of the prototype. Future work will include numerical simulations on a multistory building model to evaluate the seismic isolation system's effectiveness in employing the proposed NSD.

ACKNOWLEDGMENTS

Dai Wei acknowledges the support of the China Scholarship Council (CSC) under Grant No. 202206050096. Biagio Carboni acknowledges the support received for his work through the project "Engineered basements for vibrations protection of artworks and strategic sensitive equipment" (Grant No. 2022TH5HC2) funded by European Union—Next Generation EU within the PRIN 2022 program, D.D. 104 of the Italian Ministry of University and Research (MUR). Giuseppe Quaranta acknowledges the support received for his work through the project "Artificial Intelligence for ENVIronmental impact minimization of SEismic Retrofitting of Structures (AI-ENVISERS)" (Grant No. P20227KKF5) funded by European Union—Next Generation EU within the PRIN 2022 PNRR program, D.D. 1409 of the Italian Ministry of University and Research (MUR). This research reflects only their views and opinions and the Ministry cannot be considered responsible for them. Walter Lacarbonara acknowledges the support of the RETURN Extended Partnership, funded by the European Union Next-GenerationEU (National Recovery and Resilience Plan—NRRP, Mission 4, Component 2, Investment 1.3—D.D. 1243 PE0000005).

CONFLICT OF INTEREST STATEMENT

The authors declare no conflict of interest.

DATA AVAILABILITY STATEMENT

The data and algorithms that support the findings of this study are available from the corresponding author upon reasonable request.

ORCID

Giuseppe Quaranta https://orcid.org/0000-0001-8295-0912

REFERENCES

1. Buckle IG, Mayes RL. Seismic isolation: history, application, and performance—a world view. *Earthq Spectra*. 1990;6(2):161-201.
2. Jangid R, Datta T. Seismic behaviour of base-isolated buildings: a state-of-the-art review. *Proc Inst Civ Eng Struct Build*. 1995;110(2):186-203.
3. Calvi PM, Calvi GM. Historical development of friction-based seismic isolation systems. *Soil Dyn Earthq Eng*. 2018;106:14-30.
4. Makris N. Seismic isolation: early history. *Earthq Eng Struct Dyn*. 2019;48(2):269-283.
5. De Luca A, Guidi LG. State of art in the worldwide evolution of base isolation design. *Soil Dyn Earthq Eng*. 2019;125:105722.
6. Erdik M, Ülker Ö, Şadan B, Tüzün C. Seismic isolation code developments and significant applications in Turkey. *Soil Dyn Earthq Eng*. 2018;115:413-437.
7. Nakamura Y, Okada K. Review on seismic isolation and response control methods of buildings in Japan. *Geoenv Dis*. 2019;6(1):1-10.
8. Clemente P, Martelli A. Seismically isolated buildings in Italy: state-of-the-art review and applications. *Soil Dyn Earthq Eng*. 2019;119:471-487.
9. Hogg SJ, Elliott DA, Maley T, Broglio S, Holden T, Giorgini S. Case studies on the practical application of resilient building technologies applied in New Zealand. *Struct Eng Int*. 2020;30(2):232-241.
10. Xu G, Guo T, Li A, et al. Seismic resilience enhancement for building structures: a comprehensive review and outlook. *Structures*. 2024;59:105738.
11. Taylor AW, Lin AN, Martin JW. Performance of elastomers in isolation bearings: a literature review. *Earthq Spectra*. 1992;8(2):279-303.
12. Buckle I, Nagarajaiah S, Ferrell K. Stability of elastomeric isolation bearings: experimental study. *J Struct Eng*. 2002;128(1):3-11.
13. Mazza F, Mazza M. Nonlinear modelling of HDRBs in the seismic analysis of retrofitted and new base-isolated RC buildings. *Structures*. 2021;33:4148-4161.
14. Mokha A, Constantinou M, Reinhorn A, Zayas VA. Experimental study of friction-pendulum isolation system. *J Struct Eng*. 1991;117(4):1201-1217.
15. Almazán JL, De La Llera JC, Inaudi JA. Modelling aspects of structures isolated with the frictional pendulum system. *Earthq Eng Struct Dyn*. 1998;27(8):845-867.
16. Fenz DM, Constantinou MC. Behaviour of the double concave friction pendulum bearing. *Earthq Eng Struct Dyn*. 2006;35(11):1403-1424.
17. Castaldo P, Palazzo B, Della Vecchia P. Seismic reliability of base-isolated structures with friction pendulum bearings. *Eng Struct*. 2015;95:80-93.

18. Zhou S, Liu Y, Jiang Z, Ren Z. Nonlinear dynamic behavior of a bio-inspired embedded X-shaped vibration isolation system. *Nonlinear Dyn*. 2022;110(1):153-175.
19. Zhou S, Hou B, Zheng L, Xu P, Yu T, Ren Z. Nonlinear property and dynamic stability analysis of a novel bio-inspired vibration isolation-absorption structure. *Nonlinear Dyn*. 2024;112(2):887-902.
20. Ou H, Sun X, Wu Q, et al. A novel bio-inspired kangaroo leg structure for low-frequency vibration isolation. *Nonlinear Dyn*. 2024;112(3):1797-1814.
21. Pu H, Liu J, Wang M, et al. Bio-inspired quasi-zero stiffness vibration isolator with quasilinear negative stiffness in full stroke. *J Sound Vib*. 2024;574:118240.
22. Meng Q, Hou L, Lin R, et al. Accurate nonlinear dynamic characteristics analysis of quasi-zero-stiffness vibration isolator via a modified incremental harmonic balance method. *Nonlinear Dyn*. 2024;112(1):125-150.
23. Xu J, Jing J. Nonlinear behavior of quasi-zero stiffness nonlinear torsional vibration isolator. *Nonlinear Dyn*. 2024;112:2545-2568.
24. Zhao F, Ji J, Cao S, Ye K, Luo Q. QZS isolators with multi-pairs of oblique bars for isolating ultralow frequency vibrations. *Nonlinear Dyn*. 2024;112(3):1815-1842.
25. Liu C, Zhang W, Yu K, Liu T, Zheng Y. Quasi-zero-stiffness vibration isolation: designs, improvements and applications. *Eng Struct*. 2024;301:117282.
26. Li H, Li Y, Li J. Negative stiffness devices for vibration isolation applications: a review. *Adv Struct Eng*. 2020;23(8):1739-1755.
27. Chai Y, Bian J, Li M. A novel quasi-zero-stiffness isolation platform via tunable positive and negative stiffness compensation mechanism. *Nonlinear Dyn*. 2024;112(1):101-123.
28. Niu MQ, Chen LQ. Analysis on nonlinear stiffness isolators revealing damping thresholds. *Commun Nonlinear Sci Numer Simul*. 2024;128:107536.
29. Molyneux W. *Supports for vibration isolation*. ARC/CP-322. Aeronautical Research Council.
30. Lee CM, Goverdovskiy V, Temnikov A. Design of springs with "negative" stiffness to improve vehicle driver vibration isolation. *J Sound Vib*. 2007;302(4-5):865-874.
31. Tu L, Ning D, Sun S, et al. A novel negative stiffness magnetic spring design for vehicle seat suspension system. *Mechatronics*. 2020;68:102370.
32. Shi X, Shi W, Xing L. Performance analysis of vehicle suspension systems with negative stiffness. *Smart Struct Syst*. 2019;24(1):141-155.
33. Suman S, Balaji P, Selvakumar K, Kumaraswamidhas L. Nonlinear vibration control device for a vehicle suspension using negative stiffness mechanism. *J Vib Eng Technol*. 2021;9:957-966.
34. Shi X, Zhu S, Ni YQ, Li J. Vibration suppression in high-speed trains with negative stiffness dampers. *Smart Struct Syst*. 2018;21(5):653-668.
35. Hua Y, Zhu S, Shi X. High-performance semiactive secondary suspension of high-speed trains using negative stiffness and magnetorheological dampers. *Veh Syst Dyn*. 2022;60(7):2290-2311.
36. Sarlis AA, Pasala DTR, Constantinou M, Reinhorn A, Nagarajaiah S, Taylor D. Negative stiffness device for seismic protection of structures. *J Struct Eng*. 2013;139(7):1124-1133.
37. Sarlis A, Pasala D, Constantinou MC, Reinhorn AM, Nagarajaiah S, Taylor DP. Negative stiffness device for seismic protection of structures: shake table testing of a seismically isolated structure. *J Struct Eng*. 2016;142(5):04016005.
38. Cimellaro GP, Domaneschi M, Warn G. Three-dimensional base isolation using vertical negative stiffness devices. *J Earthq Eng*. 2020;24(12):2004-2032.
39. Alhan C, Öncü-Davas S. Performance limits of seismically isolated buildings under near-field earthquakes. *Eng Struct*. 2016;116:83-94.
40. Güneş N. Effects of near-fault pulse-like ground motions on seismically isolated buildings. *J Build Eng*. 2022;52:104508.
41. Quaranta G, Mollaioli F. On the use of the equivalent linearization for bilinear oscillators under pulse-like ground motion. *Eng Struct*. 2018;160:395-407.
42. Quaranta G, Angelucci G, Mollaioli F. Near-fault earthquakes with pulse-like horizontal and vertical seismic ground motion components: analysis and effects on elastomeric bearings. *Soil Dyn Earthq Eng*. 2022;160:107361.
43. Chen P, Wang B, Dai K, Li T. Analytical and numerical investigations of base isolation system with negative stiffness devices. *Eng Struct*. 2022;268:114799.
44. Cao S, Ozbulut OE, Shi F, Deng J. An SMA cable-based negative stiffness seismic isolator: development, experimental characterization, and numerical modeling. *J Intell Mater Syst Struct*. 2022;33(14):1819-1833.
45. Moghadam SR, Konstantinidis D. Finite element study of the effect of support rotation on the horizontal behavior of elastomeric bearings. *Comp Struct*. 2017;163:474-490.
46. Vaiana N, Spizzuoco M, Serino G. Wire rope isolators for seismically base-isolated lightweight structures: experimental characterization and mathematical modeling. *Eng Struct*. 2017;140:498-514.
47. De Domenico D, Ricciardi G, Benzoni G. Analytical and finite element investigation on the thermo-mechanical coupled response of friction isolators under bidirectional excitation. *Soil Dyn Earthq Eng*. 2018;106:131-147.
48. Bianco V, Monti G, Pio Belfiore N, Vailati M. Multibody kinematics of the double concave curved surface sliders: from supposed compliant sliding to suspected stick-slip. *Pract Period Struct Des Constr*. 2021;26(3):04021024.
49. Mezghani F, Rincónd AF, Fernandez PG, Juan dA, Sanchez-Espiga J, Rueda FV. Effectiveness study of wire mesh vibration damper for sensitive equipment protection from seismic events. *Mech Syst Signal Process*. 2022;164:108160.
50. Wang Q, Zeng J, Wei L, Zhu B. Carbody vibrations of high-speed train caused by dynamic unbalance of underframe suspended equipment. *Adv Mech Eng*. 2018;10(12):1687814018818969.
51. Mahalingam I, Padmanabhan C. A novel alternate multibody model for the longitudinal and ride dynamics of a tracked vehicle. *Veh Syst Dyn*. 2021;59(3):433-457.
52. Roupa I, Gonçalves SB, Silva dMT. Kinematics and dynamics of planar multibody systems with fully Cartesian coordinates and a generic rigid body. *Mech Mach Theory*. 2023;180:105134.
53. Dopico Dopico D, López Varela Á, Luaces Fernández A. Augmented Lagrangian index-3 semi-recursive formulations with projections: kinematics and dynamics. *Multibody Syst Dyn*. 2021;52:377-405.
54. Khadim Q, Kaikko EP, Puolatie E, Mikkola A. Targeting the user experience in the development of mobile machinery using real-time multibody simulation. *Adv Mech Eng*. 2020;12(6):1687814020923176.
55. Rodríguez AJ, Sanjurjo E, Pastorino R, Naya MÁ. State, parameter and input observers based on multibody models and Kalman filters for vehicle dynamics. *Mech Syst Signal Process*. 2021;155:107544.
56. Yu X, Mikkola A, Pan Y, Escalona JL. The explanation of two semi-recursive multibody methods for educational purpose. *Mech Mach Theory*. 2022;175:104935.
57. Bae DS, Haug EJ. A recursive formulation for constrained mechanical system dynamics: part II. Closed loop systems. *J Struct Mech*. 1987;15(4):481-506.
58. García Jalón dJ, Álvarez E, De Ribera F, Rodríguez I, Funes F. A fast and simple semi-recursive formulation for multi-rigid-body systems. In: Ambrósio JA, ed. *Advances in Computational Multibody Systems*. Springer; 2005:1-23.
59. Salvatore A, Carboni B, Lacarbonara W. *Multidirectional hysteretic damper with negative stiffness*. Italian Patent N 102021000025130 (2021-09-30), PCT/IB2022/059325 (2022-09-30) (E0141674); 2021.
60. Salvatore A, Carboni B, Lacarbonara W. Nonlinear dynamic response of an isolation system with superelastic hysteresis and negative stiffness. *Nonlinear Dyn*. 2022;107:1765-1790.

61. Wieleba W. The statistical correlation of the coefficient of friction and wear rate of PTFE composites with steel counterface roughness and hardness. *Wear*. 2002;252(9-10):719-729.
62. Shabana AA. *Dynamics of Multibody Systems*. Cambridge University Press; 2020.
63. Pan Y, Dai W, Xiong Y, Xiang S, Mikkola A. Tree-topology-oriented modeling for the real-time simulation of sedan vehicle dynamics using independent coordinates and the rod-removal technique. *Mech Mach Theory*. 2020;143:103626.
64. Jalón dJG. Twenty-five years of natural coordinates. *Multibody Syst Dyn*. 2007;18:15-33.
65. Jalon GdJ, Callejo A, Hidalgo AF. Efficient solution of Maggi's equations. *J Comput Nonlinear Dyn*. 2012;7:2.
66. Callejo A, Pan Y, Ricón JL, Kövecses J, Jalón GdJ. Comparison of semirecursive and subsystem synthesis algorithms for the efficient simulation of multibody systems. *J Comput Nonlinear Dyn*. 2017;12(1):011020.
67. Charalampakis AE, Tsiatas GC. A simple rate-independent uniaxial shape memory alloy (SMA) model. *Front Built Environ*. 2018;4:46.
68. Carboni B, Lacarbonara W, Auricchio F. Hysteresis of multiconfiguration assemblies of nitinol and steel strands: experiments and phenomenological identification. *J Eng Mech*. 2015;141(3):04014135.

AUTHOR BIOGRAPHIES

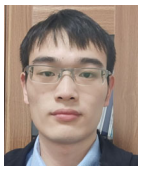

Wei Dai is a PhD candidate in Mechanical Engineering at the College of Mechanical and Vehicle Engineering, Chongqing University, China. His research interests are multibody system dynamics, structural dynamics, and vehicle dynamics.

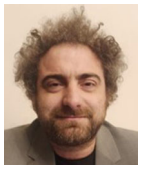

Biagio Carboni is an associate professor of structural mechanics at the Department of Structural and Geotechnical Engineering of Sapienza University of Rome. Since January 2023, he has served as the Scientific Director of the Materials and Structures Laboratory in the Faculty of Civil and Industrial Engineering. works, He was a member of the board of directors of the International Society of Nonlinear Dynamics (NODYS) until December 2023. Since May 2024, he has been a member of the board of directors of the Italian Society of Structural Mechanics (SISCo). He has been part of the organizing committee for the first, second, and third International Nonlinear Dynamics Conferences (NODYCON). His research activities focus on the general field of nonlinear structural dynamics, with both theoretical and experimental developments. Specifically, he works on vibration control, dynamic identification, damage detection, phenomenological models for hysteretic behaviors, mechanical modeling of structural systems with geometric and material nonlinearities, and the design and development of innovative structures and devices. He is the co-author of three international patents and has contributed over 40 scientific including journal articles, book chapters, and conference proceedings.

Giuseppe Quaranta is an associate professor of structural engineering at the Department of Structural and Geotechnical Engineering, Sapienza University of Rome, Italy. He also holds the National Scientific Habilitation for the position of full professor in Structural Engineering. His research focuses on structural monitoring, structural control, and concrete structures. To date, he has contributed to over 70 articles published in international peer-reviewed journals within these research areas. His research was funded by national and international bodies (NSF, European Commission, Italian Ministry for Universities and Research).

Yongjun Pan is an associate professor at the College of Mechanical and Vehicle Engineering, Chongqing University, China. He is a member of the Committee of Multibody Dynamics and Control of the Chinese Society of Theoretical and Applied Mechanics (CSTAM) and the Committee of System Simulation of the Chinese Association of Automation (CAA). His main research interests include electric vehicle dynamics and control, batteries, multibody system dynamics, and so forth. He has published over 40 articles, including 30 papers as the first or corresponding author.

Walter Lacarbonara is a professor of nonlinear dynamics at Sapienza University and Director of the Sapienza Center for Dynamics. During his graduate education, he was awarded an MS in Structural Engineering (Sapienza University), an MS in Engineering Mechanics (Virginia Tech, USA), and a PhD in Structural Engineering (Sapienza/Virginia Tech). His research interests cover nonlinear structural dynamics, metamaterials, nanocomposites, asymptotic techniques, nonlinear vibration control, experimental nonlinear dynamics, and dynamic stability of structures. He is the Editor-in-Chief of *Nonlinear Dynamics*, and a former Associate Editor for the *ASME Journal of Applied Mechanics*, *Journal of Vibration and Acoustics*, and *Journal of Sound and Vibration*. He is the chair of the International Society of Nonlinear Dynamics (NODYS). He has served as chair of the ASME Technical Committee on Multibody System and Nonlinear Dynamics, and as a General co-chair and technical program co-chair of the ASME 2015 (Boston, USA) and 2013 (Portland, USA) IDETC Conferences. He has organized over 10 international symposia/conference sessions and, very recently, the first, second, third, and fourth International Nonlinear Dynamics Conferences (NODYCON). His research is supported by national and international sources (EOARD/AFOSR, NSF, European Commission, Italian Ministry of

Science and Education). He has published over 280 papers and conference proceedings, five international patents (EU/USA/China), 30 book chapters, nine co-edited Springer books, and a single-authored book (Nonlinear Structural Mechanics, Springer) for which he received the 2013 Texty Award nomination by Springer US.

How to cite this article: Dai W, Carboni B, Quaranta G, Pan Y, Lacarbonara W. Nonlinear response of a multidirectional negative-stiffness isolation system via semirecursive multibody dynamic approach. *Int J Mech Syst Dyn*. 2024;1-20. doi:10.1002/msd2.12118